RESEARCH ARTICLE SUMMARY

NEUROPHYSIOLOGY

Brain-wide topographic coordination of rotating waves

Zhiwen Ye*, Alexander E. Ladd, Nancy MacKenzie, Ljuvica Kolich, Anna J. Li, Daniel Birman, Matthew S. Bull, Tanya L. Daigle, Bosiljka Tasic, Hongkui Zeng, Nicholas A. Steinmetz*

Full article and list of author affiliations: https://doi.org/10.1126/science.adx1369

INTRODUCTION: Electrical activity in the brain often travels in waves, propagating across networks of neurons in patterns that have been linked to sensory perception, memory, and movement. However, the spatial organization of these waves across the brain, the anatomical circuits that give rise to them, and their brain-wide distribution have remained unclear. Understanding these properties is essential for determining the roles that traveling waves may play in behavior and cognition.

RATIONALE: We combined fast, large-scale imaging of neural activity across the mouse cortical surface with high-density electrode recordings in deeper brain structures. This allowed us to track the propagation of traveling waves across the entire cortex while simultaneously measuring the spiking activity of neurons in subcortical regions including the thalamus, striatum, and midbrain. We also examined the axonal architecture of cortical neurons using three-dimensional reconstructions of their axonal projections, tested the causal role of these circuits within the somatosensory cortex, and measured wave occurrence in different brain states and behavioral contexts.

RESULTS: We discovered that rotating waves, which propagate along a circular trajectory, were a prominent and frequently occurring feature of cortical activity, predominantly centered on the somatosensory cortex. These waves therefore swept sequentially across the maps of the mouse body surface. The local wiring of neurons in this region displayed a matching circular arrangement, and a computational model confirmed that this architecture supports rotating wave formation. Across the cortex, rotating waves were mirrored between the left and right hemispheres and between sensory and motor areas, reflecting the pattern of long-range connections between these regions. Severing local circuits within the somatosensory cortex reduced rotating waves in the motor cortex, establishing a mechanistic basis. Subcortical neurons in the thalamus, striatum, and midbrain tracked cortical rotating waves on a moment-to-moment basis in their spiking patterns. Rotating waves were modulated by arousal, evoked by sensory stimulation, and selectively recruited during correct performance of a visual-motor task.

CONCLUSION: These findings reveal that brain activity is shaped by the physical architecture of neural wiring into coordinated rotating waves that span cortical and subcortical regions. Rather than being confined to isolated brain areas, these waves represent a distributed organizational principle in which the direction and timing of activity propagation are dictated by the geometry of axonal connections. The recruitment of rotating waves during different behavioral contexts suggests that they may serve as a mechanism for coordinating information flow across sensory and motor systems during perception and action. □

*Corresponding author. Email: yezhiwen10@gmail.com (Z.Y.); nick.steinmetz@gmail.com (N.A.S.) Cite this article as Z. Ye *et al.*, *Science* **392**, eadx1369 (2026). DOI: 10.1126/science.adx1369

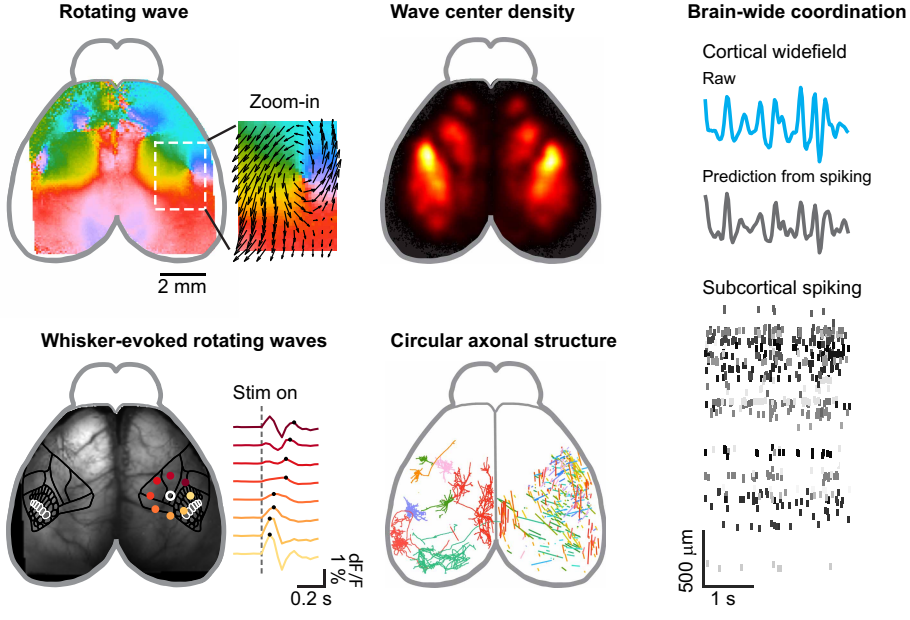

Rotating waves in mouse cortex. Neural activity forms rotating waves centered on the somatosensory cortex, sweeping across somatotopic maps of the mouse body. These waves are shaped by the circular architecture of axonal connections, mirrored across hemispheres, coordinated with subcortical regions, and recruited in different behavioral contexts.

NEUROPHYSIOLOGY

Brain-wide topographic coordination of rotating waves

Zhiwen Ye[1]*, Alexander E. Ladd[1], Nancy MacKenzie[1], Ljuvica Kolich[1], Anna J. Li[1], Daniel Birman[1], Matthew S. Bull[2]†, Tanya L. Daigle[2], Bosiljka Tasic[2], Hongkui Zeng[2], Nicholas A. Steinmetz[1]*

Patterns of brain activity moving in waves occur across brain regions and species, yet their spatial organization, anatomical basis, and brain-wide distribution remain unclear. Using cortex-wide imaging and electrophysiology in awake mice, we revealed a prominent wave motif across spatial scales. Waves frequently formed rotational patterns centered on somatosensory cortex and sweeping across somatotopic maps. Axonal architecture within sensory cortex exhibited a matching circular arrangement. Rotating waves were mirrored between hemispheres and between sensory and motor cortex and were coordinated with subcortical spiking. Bilaterally cutting the circular circuitry diminished rotating waves. Rotating waves were modulated across behavioral states, evoked by sensory inputs, and recruited during correct visuomotor performance. These results establish that rotating waves are sculpted by axonal architecture across diverse brain systems and behavioral contexts.

Rotating waves, also called vortices or spiral waves, are dynamic patterns of brain activity (*1*–*4*) previously observed across various timescales and species, including turtles (*5*), mice (*6*–*9*), rats (*10*), cats (*11*), monkeys (*12*–*14*), and humans (*15*–*21*). Traveling waves, including rotating waves, are strongly correlated with a variety of perceptual, cognitive, and motor behaviors (*12*, *22*–*34*). Previous studies of such waves often relied on measures of neural activity at restricted temporal (*16*, *17*) or spatial (*12*, *15*, *22*) resolutions and scales, limiting their ability to identify organizational principles and link these dynamic patterns with underlying features of the neural architecture.

Within the cortex, sensory processing is traditionally viewed as modular and hierarchical, with information processed in parallel sensory systems (visual, auditory, whisker, etc.) and integrated in higher-order association areas (*35*). Although evidence suggests that multisensory integration occurs at the primary sensory cortical level, such as auditory-visual (*36*, *37*) and visual-somatosensory interactions (*38*, *39*), these few well-studied pathways may constitute only a fraction of the interactions between low-level sensory areas (*39*). Adjacent sensory areas (upper limb, lower limb, mouth, nose, etc.) in mammals form a somatotopic homunculus (*40*–*42*), but the extent to which activity propagates across these regions remains largely unknown.

Considering a broader spatial scale, prior studies of traveling waves in mammals have primarily focused on waves in isolated brain regions, especially neocortex (*5*, *7*, *10*, *12*, *15*, *17*, *22*, *24*, *29*, *30*), hippocampus (*26*–*28*), and others (*25*, *43*). Despite the known anatomical (*41*, *44*–*46*) and functional (*47*–*49*) connectivity among the neocortex, thalamus, basal ganglia, and midbrain, it remains unclear whether fast-traveling waves, on the subsecond timescale of perception and action, are topographically coordinated in relation to long-range connectivity in the adult brain (*8*, *50*–*54*). The mere existence of axonal projections from one brain region to another does not imply that all patterns of activity are transmitted from one region to the other. Specifically, traveling waves could be in the "null space" of activity; that is, they could be patterns of activity that are not transmitted to target areas (*55*, *56*), for example, if projection neurons do not encode traveling waves. Whether traveling waves are indeed localized phenomena that can be adequately studied with a focus on isolated brain regions, or whether understanding their mechanisms and function requires a more distributed perspective, remains unclear.

Here, we used fast mesoscopic imaging with large-scale electrophysiology to elucidate the organization of traveling waves in the awake mouse, the features of axonal architecture underlying them, their coordination across diverse brain regions, and their functional implications for sensation and behavior.

Results

Rotating waves in mouse cortex

To investigate the mesoscale spatiotemporal dynamics of neural activity across the cortex, we performed wide-field calcium imaging in awake, head-fixed mice expressing the calcium sensors jGCaMP7 or jGCaMP8 across cortical neurons. We focused our analysis on the 2- to 8-Hz frequency range and observed prominent activity across the dorsal cortex (fig. S1, A to G). Calcium activity in this frequency range reliably captured local population spiking and local field potentials (fig. S1, H to K). These oscillations are among the most prominent fluctuations during spontaneous awake brain activity in mice (*57*–*62*). In addition, activity in the 2- to 8-Hz range includes an alpha-like 3- to 6-Hz oscillation in visual cortex (*57*, *58*, *60*) that is correlated with perceptual sensitivity in discrimination tasks (*61*) and may include homologs of the human somatosensory mu rhythm (*63*). To visualize the spatiotemporal propagation of traveling waves in this frequency range, we applied the Hilbert transform to the filtered data for each pixel independently to extract the oscillation phase at each moment in time (Fig. 1A).

We consistently observed rotating waves, which exhibited a circular arrangement of oscillation phases, in the wide-field imaging data (Fig. 1, A to C; figs. S1 and S2; and movie S1). Spontaneous oscillations and dynamics in awake animals are nonstationary and complex, with nonuniform and changing oscillation frequency and amplitude over space and time. To robustly characterize their properties, we designed an automated rotating wave detection algorithm (fig. S2, A to E). Rotating waves could occur randomly within spatiotemporally correlated data, with phase progression arising artificially when filtering or smoothing is applied to spatially discrete activations (*17*, *64*). To determine whether the observed rotating waves occurred more frequently than expected by chance, we constructed three-dimensional (3D) surrogate data with a Fourier phase shuffling method (see the Materials and methods) in which the spatial and temporal autocorrelations of the data were preserved (*17*, *65*). Whereas small rotating waves commonly occurred by chance in the shuffled data, large rotating waves (radius ≥40 pixels, or 0.69 mm) occurred in the original data more often than in the shuffled data across sessions and were therefore included for further analysis (fig. S3, A to E). Rotating waves formed sequences persisting for tens to hundreds of milliseconds (Fig. 1, B and D). Because single-frame rotating waves occurred frequently by chance in permuted data (Fig. 1D), we focused further analyses on wave sequences lasting multiple sampling frames (≥57 ms; Fig. 1D). Rotating waves were also observed in mice that expressed calcium-sensitive fluorescent proteins only in neuron somas and proximal dendritic segments (fig. S4), indicating that they reflected patterns of local activity rather than axonal inputs.

The rotating wave activity patterns that we observed were consistently localized, frequently occurring, and had a characteristic rotational speed. Most rotating waves swept across the somatotopic maps

[1]Department of Neurobiology & Biophysics, University of Washington, Seattle, WA, USA. [2]Allen Institute for Brain Science, Seattle, WA, USA. ***Corresponding author. Email: yezhiwen10@gmail.com (Z.Y.); nick.steinmetz@gmail.com (N.A.S.)** †Present address: Unconventional Inc., Palo Alto, CA.

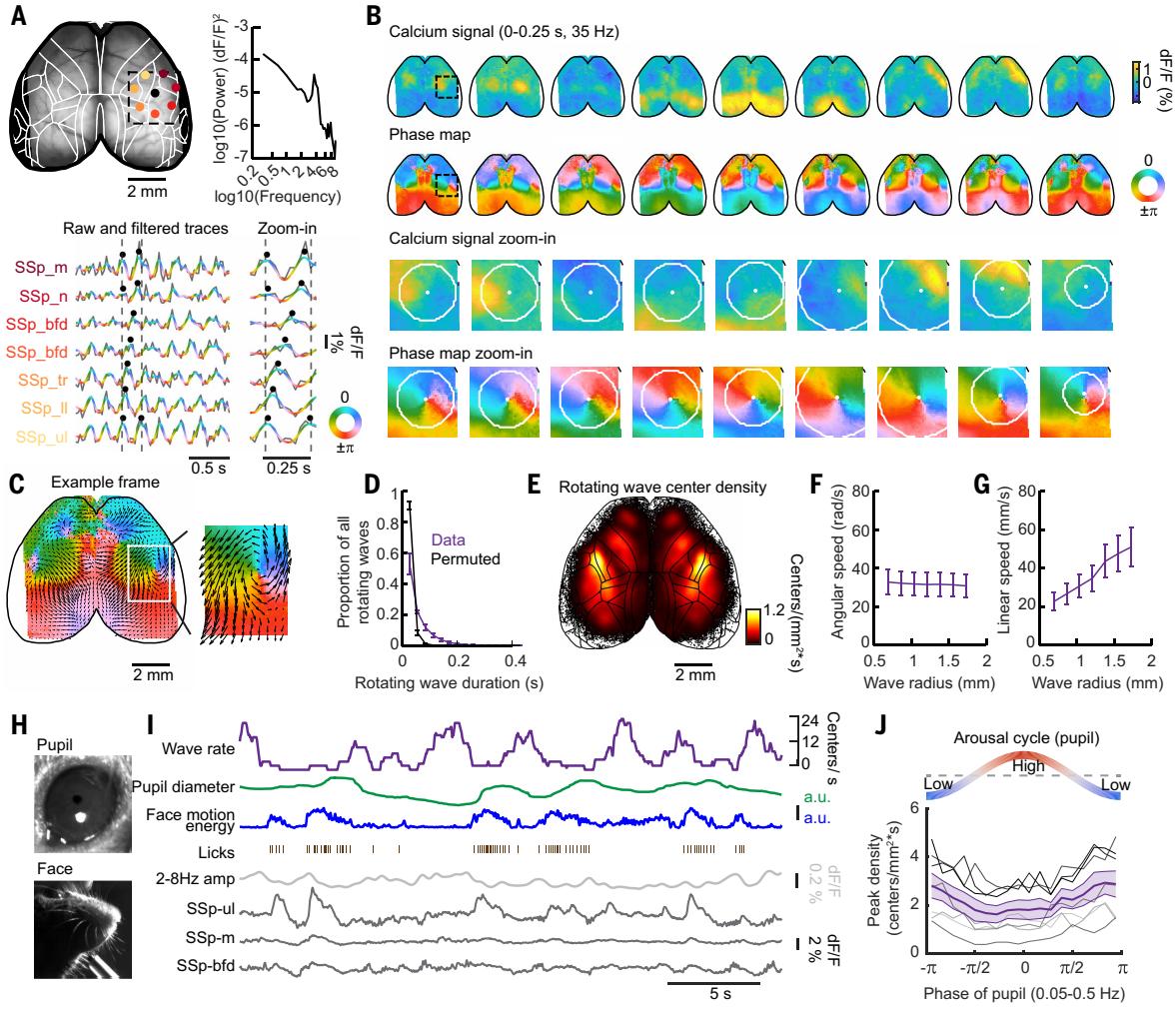

Fig. 1. Rotating waves are prevalent in the neural dynamics of mouse cortex. (**A**) Top left: example pixels from calcium imaging of the dorsal cortical surface. Top right: average power spectrum of the example traces. Bottom: raw traces (gray) are overlaid with 2- to 8-Hz filtered traces color coded by phase values. (**B**) Nine example consecutive frames (0.25 s) of calcium signal maps, phase maps and their zoom-in maps, within the time window indicated by the dashed lines in (A). (**C**) Phase map from an example frame with a rotating wave, and optical flow overlaid depicting wave direction. (**D**) Durations of rotating waves in data (purple) and in permuted data (black). Error bar indicates SEM ($n = 15$ mice). (**E**) Density estimate of rotating wave center distribution ($n = 15$ mice). (**F**) Angular speed distribution as a function of rotating wave radius across 15 mice. (**G**) Linear speed of rotating waves as a function of rotating wave radius. (**H**) An example frame of pupil video and face video. (**I**) An example epoch of recording with neural activity, behavior parameters, and rotating wave rates. Rotating wave rate and 2- to 8-Hz amplitude traces are smoothed with a 1-s window. (**J**) Peak density of rotating waves as a function of the phase of pupil diameter fluctuations within 0.05 to 0.5 Hz. Gray traces indicate individual mice that have pupil-tracking data (7/15 mice). SSp_bfd, _n, _m, _tr,_ll, _ul indicates primary somatosensory area, barrel field, nose, mouth, trunk lower limb, upper limb; RSP, retrosplenial cortex; VISp, primary visual cortex.

of the mouse body representation sequentially, including lower limb, upper limb, mouth, nose, and the barrel field (Fig. 1, A to C, and fig. S2). Rotating wave centers were highly concentrated in the middle of primary somatosensory cortex (SSp) across animals (Fig. 1E), a property observed across different mouse lines (fig. S4), rotating wave sizes, and durations (fig. S5). Rotating waves had a peak rate of 1.2 rotating wave centers/mm^2/s on average, or 3.4% of frames/mm^2 at 35 Hz (Fig. 1E and fig. S4; $n = 15$ mice). Rotating wave centers often drifted within a rotating wave sequence and were slightly more likely to rotate counterclockwise in the right hemisphere (fig. S6, A and B). Plane waves were also observed in our data (fig. S7), consistent with previous reports (*7*, *66*). Frames with a high plane wave index typically had a low rotation index and vice versa (fig. S7, A to F). With improved kinetics of calcium sensors and improved spatial resolution in soma-targeting jGCaMP8m compared with jGCaMP7 (*67*–*69*), the occurrence of detected rotating waves increased (jGCaMP8m: 10 ± 0.9%; jGCaMP7: 2 ± 0.2%), whereas plane waves decreased (jGCaMP8m: 13 ± 0.9%; jGCaMP7: 23 ± 2%; figs. S4 and S7Q). Rotating waves had consistent angular speed (ω) across different radii (31.9 ± 6.1 rad/s, mean ± SD, equivalent to 5.1 ± 1.0 Hz; Fig. 1F and fig. S8) but increasing linear speed as a function of radius (Fig. 1G and fig. S8). The propagation speeds of these waves (0.05 ± 0.01 m/s at 1.7 mm rotating wave radius, mean ± SD) are therefore substantially slower than axonal conduction velocities, which are on the order of 0.5 to 1.5 m/s for lateral unmyelinated axons in neocortex (*70*, *71*) and likely reflect axon conduction across multiple connections. Similar rotating wave patterns were observed within the 0.05- to 0.5-Hz and 0.5- to 2-Hz frequency bands at greater rates compared with shuffle controls but lower than rates in the 2- to 8-Hz range (fig. S3, F and G).

Rotating wave rates varied across arousal cycles as measured with pupil diameter fluctuations (Fig. 1, H and I). Rotating wave occurrence was significantly correlated with the phase of slow (0.05 to 0.5 Hz) pupil diameter fluctuations (rho = 0.47, $P < 0.001$; circular-linear correlation), with higher rates during low-arousal quiescent states (Fig. 1,

I and J; low versus high: 3.4 ± 0.7 versus 1.7 ± 0.4 centers/mm^2/s; P = 0.003, paired Student's t test). Similar results were obtained using face motion energy (fig. S6, K to N).

An axonal basis for rotating waves in sensory cortex

To investigate the anatomical basis for the propensity of rotating waves to form around the somatosensory cortex, we examined the local axonal architecture of neurons in sensory cortex. Using an open dataset of cortical neuron reconstructions (*72*), we discovered that local axons from mouse cortical neurons were also organized circularly (Fig. 2, A to C). In particular, the major axes of the axonal terminals from single neurons aligned almost perpendicularly to the vector from the SSp center to the soma location (Fig. 2, C and E; 87.4°, n = 435 neurons; 95% confidence interval for circular t test = 82.8° to 92°, P < 0.05; real data versus permutation distribution: P < 0.05, Watson's U^2 test). Moreover, the orientation of these axonal axes matched the propagation directions of rotating waves, exceeding a permuted distribution of flow vectors (Fig. 2, D and F; P = 0.004, Student's t test). We did not observe a circular arrangement of axons in motor cortex, although there was a nonrandom organization with a bias in the anterior-posterior direction (fig. S9, A to D). Neurons in both the superficial and deep layers of the sensory cortex exhibited circular organization around the middle of somatosensory cortex (fig. S9, E to H). Moreover, axonal length of single neurons along the tangential (circular) axis increased with soma-to-SSp-center distance (Fig. 2, G and H), with a correlation coefficient significantly higher than the permutation distribution (r = 0.49; P < 0.001, Student's t test). This feature may have contributed to the faster linear wave speed observed at larger radii (Fig. 1, F and G). The circular axonal architecture was centered on a localized region within SSp rather than on a singular point (fig. S9, I to K), which may account for the moment-to-moment variability in rotating wave centers (*73*, *74*).

A computational simulation of activity propagation over sheets of cortical neurons, modeled as coupled oscillators (*75*–*77*) with circularly

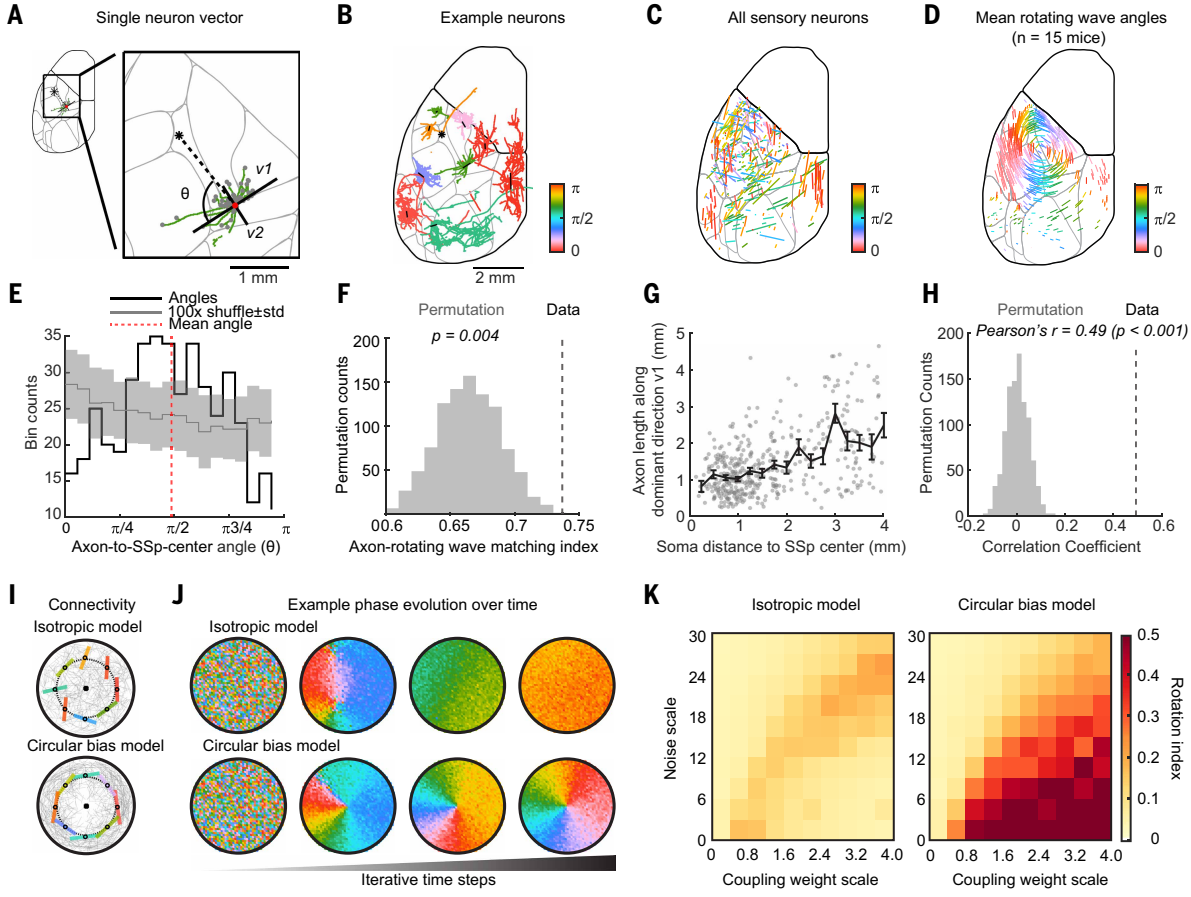

Fig. 2. Axon orientations of single neurons match the circular arrangement of rotating waves around the middle of somatosensory cortex. (**A**) Morphology of an example neuron's axonal arbor (green) with local axon terminals overlaid (gray). The top two singular vectors of the terminal point cloud (v_1, v_2; black) are overlaid on top of the axonal arbor and centered on the soma (red). Asterisk represents the middle of SSp. Axon-to-SSp-center angle (θ) is the angle between the first singular vector (v_1) and the vector from the soma to the SSp middle. (**B**) Axonal arbors of nine example neurons. The direction of the vector overlaid (black) represents the first singular vector. The length of the vector represents axonal arbor polarity (see the Materials and methods) centered on the cell soma positions. (**C**) Axon orientation and polarity for all sensory neurons (n = 435 neurons), as in (B). Color represents the angle of the vectors. (**D**) Mean activity flow vectors of a collection of large rotating waves with the same direction of rotation across mice (n = 15). (**E**) Histogram of axon-to-SSp-center angle (θ) for all 435 neurons. The mean angle is indicated by the dashed red line. Mean and SD of shuffled distribution is indicated in gray. (**F**) Axon-flow matching index of the data relative to the permutation distribution. (**G**) Relationship between axon length along v_1 direction [see panel (A)] and soma distance to SSp center. Each dot represents a single neuron. Black trace, mean axon length within 0.25-mm distance bins from SSp center, mean ± SEM. (**H**) Correlation between axon lengths and distances to the SSp center of single neurons relative to the permutation distribution. (**I**) Connectivity diagram for the isotropic model and circular bias model. The primary vectors of the connection clouds for eight example oscillators are overlaid on top of all connection pairs (gray). (**J**) Example phase map progression in the isotropic (top) and circular bias model (bottom) under the same random initial conditions. (**K**) Rotation index (see the Materials and methods) as a function of coupling weight scale and noise scale in the isotropic model (left) and circular bias model (right).

biased connectivity as in the data (see the Materials and methods), exhibited strengthened rotating wave dynamics relative to a model with isotropic connectivity (Fig. 2, I and J). As reported previously (*1*, *78*–*80*), traveling waves naturally emerged when coupling was local and sufficiently strong to synchronize neighboring oscillators. In the isotropic model, rotating waves were most prevalent near the transition between desynchronized and synchronized regimes (Fig. 2K), consistent with topological defects in 2D phase oscillator systems that can transiently stabilize (*81*, *82*). By contrast, in the circular bias model, where circular connectivity was imposed, rotating waves were stabilized and centered at even higher coupling strengths (Fig. 2K and fig. S10, A to E). Therefore, the anatomical architecture of axons in the somatosensory cortex corresponds to the rotating waves that we observed and could support the occurrence of these dynamic patterns.

Topographically mirrored rotating waves across the cortex

Rotating waves were often symmetrical between the left and right hemispheres, as well as between sensory and motor cortex, reflecting across the border of primary somatosensory cortex (SSp) and primary motor cortex (MOp). When two rotating waves were detected simultaneously in mirrored brain structures (SSp-MOp, SSp-left-right, MOp-left-right), they mostly traveled in opposite directions (Fig. 3A; for a full comparison, see fig. S6F), with no substantial time lags across mirrored areas (fig. S11, C and D).

To account for the observed phase map symmetry (Figs. 1B and 3A), we used reduced rank regression to predict activity across hemispheres and across the sensory-motor border (Fig. 3B). We included visual (VIS) and retrosplenial (RSP) cortex in this analysis because these areas were often incorporated into global dynamics (Figs. 1B and 2). Reduced-rank regression with 16 latent components explained 98 ± 0.1% of the variance in

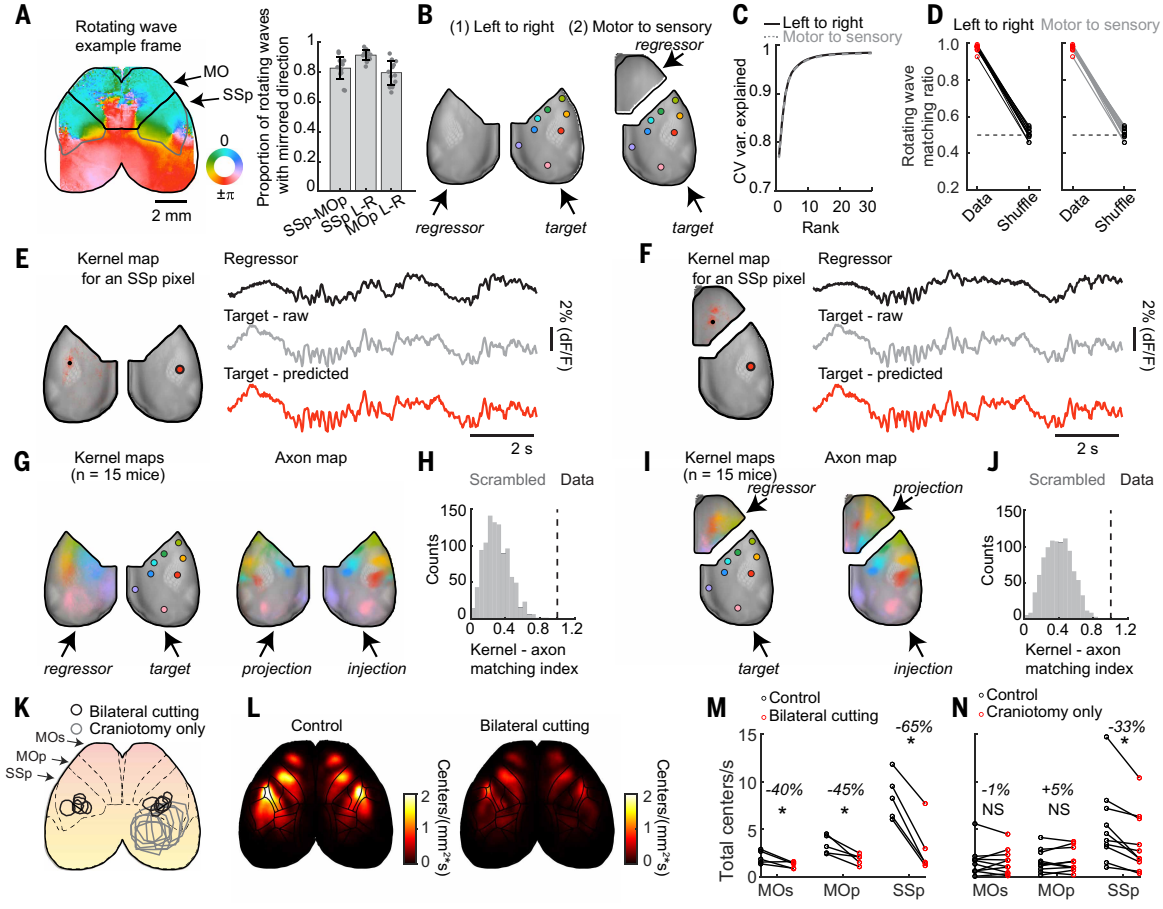

Fig. 3. Rotating waves are mirrored between hemispheres and between sensory and motor cortex, reflecting underlying topographic mapping of activity and long-range axons. (**A**) Left: an example phase map with SSp-MOp border depicted in black outline. Right: proportion of paired rotating waves with mirrored direction between topographically connected cortical regions (SSp-MOp, within hemisphere; SSp L-R and MOp L-R, opposite hemispheres). (**B**) Schematic of regressions to predict right sensory cortical activity from (1) left sensory cortex and (2) right hemisphere motor cortex. Centers of eight sensory cortical regions are highlighted in colored dots. (**C**) Cumulative cross-validated variance explained as a function of rank from the reduced rank regression model. (**D**) Rotating wave matching ratios comparing raw data and prediction relative to shuffled controls. (**E**) Left: regression kernel map in the left hemisphere for predicting an example right SSp-bfd pixel. Right: example regressor trace (black) with the highest regression weight from left hemisphere (top right) and raw (gray, middle right) and predicted activity trace (red, bottom right) of the example right SSp-bfd pixel. (**F**) Same as (E) but with motor cortex traces as regressors. (**G**) Left: averaged kernel maps for all example pixels in the right sensory cortex across 15 mice. Right: axon targets in the left hemisphere from viral injections in the right hemisphere. (**H**) Topographic kernel-axon matching index compared with the permutation distribution. (**I**) Same as (G) but for activity kernels of motor-to-sensory prediction and axon targets in the motor cortex from the same viral injections as in (G). (**J**) Same as (H) but for kernel maps and axon projection fields in (I). (**K**) Locations of bilateral cutting windows ($n = 5$ mice) and craniotomies in mice without cutting ($n = 9$ mice). Control data are acquired from a separate cohort with larger cranial windows prepared for combined wide-field and electrophysiology recordings. (**L**) Rotating wave center density before (left) and after (right) bilateral SSp cut. Density maps were concatenated across $n = 5$ mice. (**M**) Comparison of rotating wave rates in MOp, MOs, and SSp in bilateral cutting experiments (*$P < 0.05$, paired *t* test). (**N**) As in (M) but for sessions in which craniotomies were made without cutting.

held-out data (mean ± SEM, 15 mice; Fig. 3C). explained (mean ± SEM, 15 mice) with 16 latent components (Fig. 3C). As a result, the directions of observed and predicted rotating waves nearly always matched (97.5 ± 0.4%), whereas shuffled controls were at chance (50.9 ± 0.7%; Fig. 3D). In addition, activity of a given pixel in one hemisphere (or sensory cortex) could be represented as a linear combination of activity in the mirrored region with a spatially localized kernel map, that is, the weight matrix of a linear regression (Fig. 3, E and F). Therefore, moment-to-moment population activity is topographically shared between hemispheres, as well as between sensory and motor cortex.

Long-range cortico-cortical axonal projections matched functional kernel maps, underlying mirrored rotating waves across cortex. We computed axonal projection maps that depict the distribution of axons projecting from one region to the others, as measured with anterograde viral tracing in publicly available data (*46*). The spatial arrangement of the localized kernel maps closely matched the axonal projection maps for both interhemispheric (Fig. 3, G and H, $P = 1.6 \times 10^{-6}$; Student's t test; see the Materials and methods) and sensory-motor comparisons (Fig. 3, I and J; $P = 1.4 \times 10^{-4}$; Student's t test). Our computational model confirmed that incorporating mirrored long-range connectivity eliminated rotating wave centers near region boundaries and produced symmetrical rotating waves in mirror-connected regions (fig. S10, F to J). This mirrored topographic connectivity may also secondarily stabilize wave persistence by enforcing phase-mirrored boundary conditions that limit wave drift (fig. S10, H and I).

To causally test whether circuitry within SSp was required for rotating waves, we examined rotating waves in MO before and after making small bilateral cuts within SSp (Fig. 3K). Rotating wave occurrence was significantly reduced in both secondary (MOs; before, 2.1 ± 0.3 centers/s; after, 1.3 ± 0.1 centers/s; $P = 0.04$, $n = 5$ mice) and primary motor cortex (MOp; before, 3.4 ± 0.4 centers/s; after, 1.9 ± 0.2 centers/s; $P = 0.02$, $n = 5$ mice; Fig. 3, L and M). Craniotomies within SSp alone, without cutting, did not change rotating wave occurrence in either MOs or MOp (Fig. 3, K and N). Therefore, intact circuitry within SSp is required for normal rotating waves, and rotating waves in the motor cortex are causally dependent on SSp.

Brain-wide coordination of rotating waves

To investigate whether individual rotating waves simultaneously occur in cortex and in subcortical areas, we combined wide-field imaging in the cortex with four-shank Neuropixels electrophysiology in subcortical areas, including thalamus, striatum, and midbrain (Fig. 4A). When 2- to 8-Hz oscillations were prominent in the cortex, we consistently observed corresponding oscillations in the subcortical spiking activity (Fig. 4, B and C, and fig. S12). To test whether subcortical spiking activity contained information about cortical rotating wave propagation, we implemented a linear regression model to predict cortical activity from subcortical spiking activity. Subcortical spiking could predict cortical activity well across much, but not all, of the cortical surface (Fig. 4, B and C, and fig. S13A), presumably because the subcortical regions were incompletely sampled.

We assessed whether rotating waves were present in the activity patterns of subcortical areas by investigating whether predictions from subcortical activity recapitulated rotating waves in the cortical activity (Fig. 4, D and E, and fig. S12). Given the variability of prediction accuracy across sessions and brain regions, we took a probabilistic approach to quantify matching of rotating waves with subcortical predictions. We computed the probability that rotating waves in the

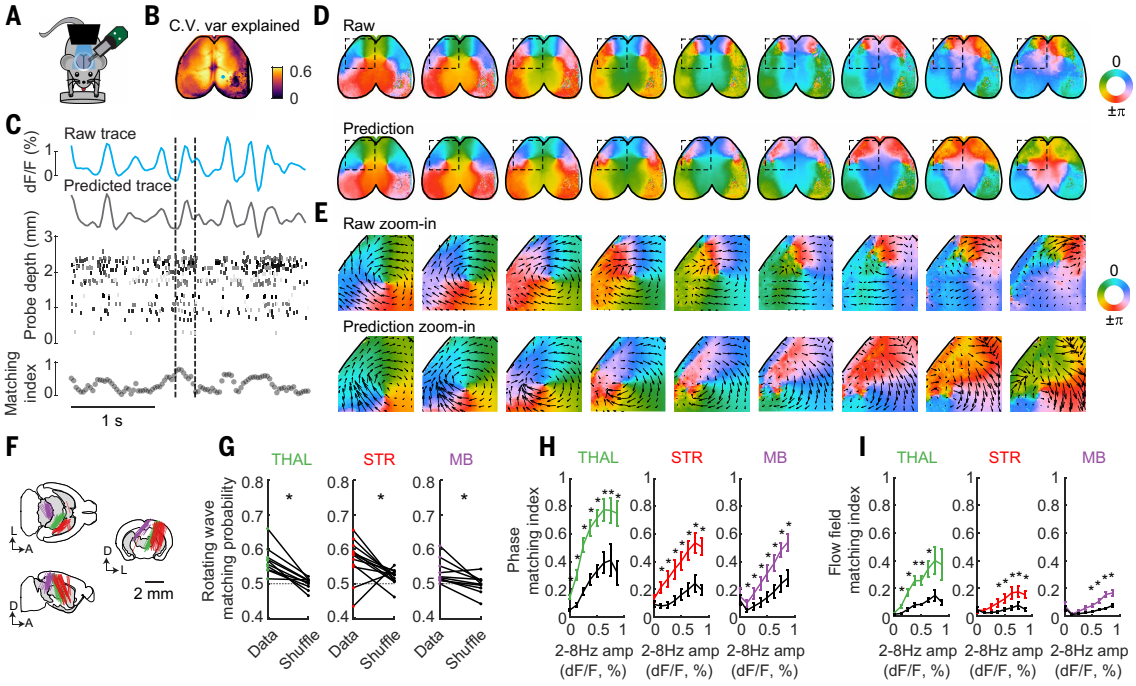

Fig. 4. Rotating waves are coordinated between cortical and subcortical regions. (**A**) Illustration of simultaneous cortical wide-field and subcortical electrophysiological recordings with four-shank Neuropixels 2.0 probes. (**B**) Example map showing cross-validated variance explained of cortical wide-field data predicted from thalamic population spiking. The craniotomy was in the right posterior cortex. (**C**) Top: example epoch of raw (blue) and predicted (gray) cortical calcium activity for an example pixel highlighted in (B). Middle: thalamic spike raster plot ordered by probe depth. The tips of the four-shank probe are at 0 mm. Each neuron is color coded by a randomized shade of gray. Bottom: traveling wave matching index between raw and predicted phase maps. (**D**) Example raw (top) and predicted (bottom) phase maps of cortical activity within the dashed lines in (C). (**E**) Magnified view of raw (top) and predicted (bottom) phase maps within the square ROI in (D) with activity flow vectors overlaid. (**F**) Probe trajectories. (**G**) Rotating wave matching probabilities between rotating waves detected from raw and predicted cortical phase maps relative to the shuffle distribution (chance, 0.5). (**H**) Phase matching indices as a function of cortical 2- to 8-Hz amplitude. Black traces represent the corresponding shuffled conditions. (**I**) As in (H) but for flow field matching index.

raw cortical frames rotated in the same direction as rotating waves in the predicted frames from all thalamic, striatal, and midbrain spiking data (Fig. 4, F and G). Rotating waves were significantly more likely to match rotation directions from prediction with the real spiking data compared with data in which neuron identities were shuffled, and the matching probability was above chance level (thalamus: 0.57 ± 0.01 versus 0.5 ± 0.01, $P = 3.8 \times 10^{-4}$; striatum: 0.57 ± 0.02 versus 0.52 ± 0.01, $P = 0.03$; midbrain: 0.53 ± 0.01 versus 0.5 ± 0.01, $P = 0.008$; mean ± SEM; paired Student's t test) for all subcortical regions (Fig. 4G). Rotating wave occurrences were modulated across arousal states, but prediction accuracy did not differ between the aroused and quiescent states (fig. S13, G and H).

To determine whether traveling waves were more generally coordinated outside of rotating waves, we quantified waves with optical flow and compared them between raw and predicted cortical activity (Fig. 4, D and E, and fig. S12). As cortical 2- to 8-Hz oscillation amplitude increased, both phase maps and traveling wave directions were more likely to match between raw cortical activity and predicted activity from all subcortical regions (Fig. 4, H and I; all $P < 10^{-4}$; main effect of 2- to 8-Hz amplitude, unbalanced two-way ANOVA). Wave matching exceeded shuffled permutations across the majority of individual sessions (fig. S13F; 10/10 sessions in thalamus, 12/12 sessions in striatum, and 9/10 sessions in midbrain) and across sessions (Fig. 4I), demonstrating that temporally ordered subcortical spiking, not just 2- to 8-Hz amplitude fluctuations, was critical for predicting cortical traveling waves. Therefore, cortical rotating waves and traveling waves are represented in subcortical brain areas on a moment-to-moment basis.

Activation of facial whiskers evokes rotating waves

Given the prevalence of rotating waves in spontaneously arising activity patterns and the anatomical basis of this pattern that we identified above, we reasoned that cortical activity in other contexts may also be organized into rotating waves. To test this, we applied brief (30-ms) air puffs near the facial whisker pad at random intervals (1 to 6 s, mean 3 s) in head-restrained mice (Fig. 5A). In the cortical barrel field of somatosensory cortex (SSp-bfd), activation first peaked at 69 ± 7 ms. Averaging across trials (1000 trials/session, $n = 5$ mice), we observed sequential progression of activity around somatosensory cortex, beginning with a high-amplitude response in SSp-bfd followed by lower-amplitude peaks at successively later time points before returning to SSp-bfd with a second peak of activation there, thus completing a full rotation (Fig. 5, B and C). Our analysis detected this as a sequence of rotating waves centered on right somatosensory cortex after stimulation of the left whisker pad, with corresponding rotating waves in the right primary and secondary motor cortex (MOp and MOs) within 300 ms of stimulus onset (Fig. 5, B and C).

On a trial-by-trial basis, the rate of detected rotating waves significantly increased in the contralateral cortex (fig. S14A; prestimulus versus poststimulus: 6.8 ± 1.0 versus 8.5 ± 0.7 centers/s, $n = 5$ mice, $P = 0.008$) and peaked at 103 ± 7 ms from stimulus onset, but not in the ipsilateral cortex (Fig. 5, D and E; prestimulus versus poststimulus: 6.5 ± 0.4 versus 6.5 ± 0.4 centers/s, $n = 5$ mice, $P = 0.93$). At later times, rotating wave occurrence significantly decreased in both hemispheres before returning to baseline (Fig. 5E; contralateral: 6.8 ± 1.0 versus 4.4 ± 1.1 centers/s at 269 ± 7 ms, $P = 0.0001$; ipsilateral: 6.5 ± 0.4 versus 5.1 ± 0.2 centers/s at 240 ± 29 ms, $P = 0.006$).

After stimulus onset, evoked rotating waves showed a clear directional bias. Rotating waves were more likely to rotate clockwise in the contralateral sensory cortex (Fig. 5F; CW wave ratio prestimulus versus poststimulus: 0.5 ± 0.02 versus 0.7 ± 0.02, $n = 5$ mice, $P = 0.003$) and slightly less likely in the ipsilateral sensory cortex (0.5 ± 0.01 versus 0.47 ± 0.01, $n = 5$ mice, $P = 0.007$). Rotating waves in the secondary motor cortex showed a similar contralateral bias (0.51 ± 0.03 versus 0.65 ± 0.04, $n = 5$ mice, $P = 0.003$), but the trend was not significant ipsilaterally (0.46 ± 0.03 versus 0.4 ± 0.07, $n = 5$ mice, $P = 0.3$).

Rotating waves in visual-motor behavior

To further understand the range of contexts in which cortical activity organizes into rotating waves, we performed cortical wide-field imaging in mice engaged in a visual-motor two-alternative choice task

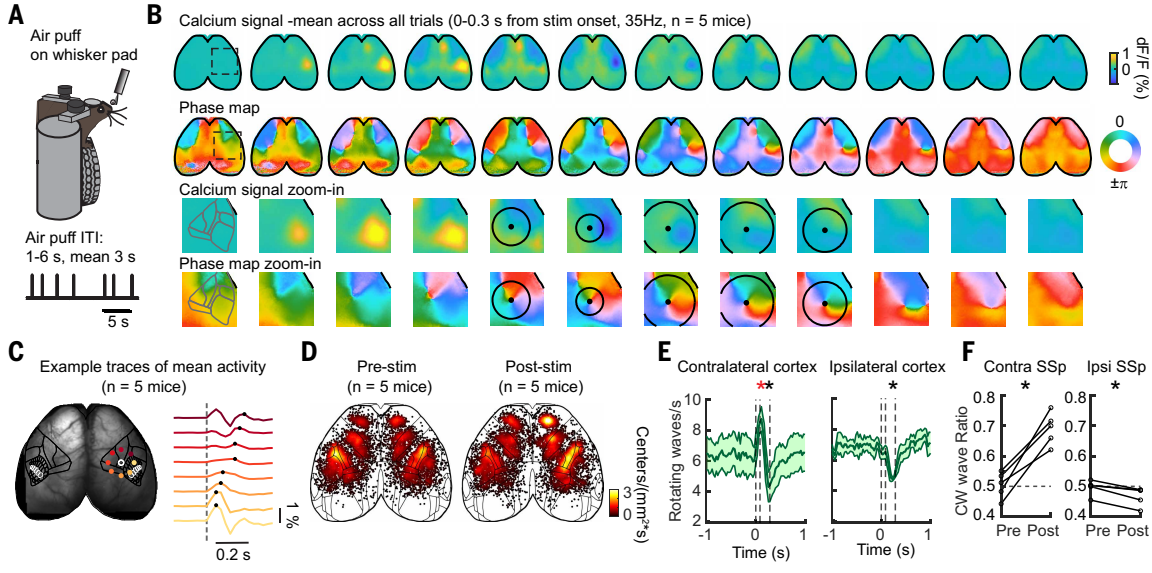

Fig. 5. Rotating waves evoked by activation of the barrel field of somatosensory cortex. (**A**) Schematic of air puff on the mouse whisker pad. (**B**) Mean calcium activity and phase map across the cortex from stimulus onset ($n = 5$ mice, 1000 trials each). (**C**) Mean calcium activity traces from evenly sampled pixels around the rotating wave center in (B). The dashed line indicates stimulus onset time. A row of barrel fields (C1 to C6) is highlighted in white. Black dots indicate peak times at each sampled location. (**D**) Rotating wave center density maps 200 ms before and after stimulus onset ($n = 5$ mice). (**E**) Rotating wave rates around stimulus onset (red asterisk, paired t test at 50 ms poststimulus; black asterisk, paired t test at 200 ms poststimulus). The dashed lines indicate times 0, 50, and 200 ms from stimulus onset. $N = 5$ mice, mean ± SEM. (**F**) Directional bias of poststimulus rotating waves.

(*83*, *84*). In this task, head-fixed mice detected a grating stimulus on the left or right side of a screen and turned a rubber wheel with their forepaws to center the stimulus, earning a water reward (clockwise for left stimulus, counterclockwise for right stimulus; Fig. 6A). Trained mice achieved high accuracy on high-contrast stimuli but showed reduced performance on low-contrast stimuli (fig. S15A; 6% contrast: 56.4 ± 6.8%; 100% contrast: 86.8 ± 9.0%; $n = 4$ mice; $P = 0.002$, paired Student's t test).

After stimulus onset, trial-averaged activity sequentially propagated across cortical areas, forming a rotating wave during correct but not incorrect or miss trials (Fig. 6, B and C, and fig. S14, B to G). Activity began with a high-amplitude peak in visual cortex, followed by activity in retrosplenial, limb somatosensory, and mouth/nose/whisker somatosensory areas before completing a full rotation with a second peak of activity in visual cortex (Fig. 6, B and C). On a single-trial basis, the total number of rotating waves did not change after stimulus onset across trial types, but several reorganizations were specific to correct trials (Fig. 6D and fig. S14K). First, wave size distributions shifted. Rotating waves with large radii more than doubled in correct trials (Fig. 6E and fig. S14K; e.g., large waves with 1.73 mm radius prestimulus versus poststimulus: 1.0 ± 0.04 versus 2.5 ± 0.4 centers/s; $P < 0.001$; $n = 4$ mice, 35 sessions; within-subject session permutation test, Bonferroni-Holm correction), whereas small waves decreased (e.g., small waves with 0.69 mm radius prestimulus versus poststimulus: 2.7 ± 0.3 versus 2.0 ± 0.2 centers/s, $P = 0.03$; $n = 4$ mice, 35 sessions). By contrast, incorrect and miss trials showed no changes across radii (fig. S14K). Second, directions of all rotating waves became significantly biased in correct trials (Fig. 6F): clockwise biased in the contralateral sensory cortex (prestimulus: 0.56 ± 0.004; poststimulus: 0.69 ± 0.02; $n = 4$ mice; $P = 0.01$) and counterclockwise biased in the ipsilateral sensory cortex (prestimulus: 0.46 ± 0.03; poststimulus: 0.31 ± 0.02; $n = 4$ mice; $P = 0.003$). No directional changes occurred in incorrect or miss trials. Third, the spatial peak of rotating waves shifted from the middle to the bottom of SSp, closer to the posterior parietal cortex (PPC) (Fig. 6, B and D), consistent with increased engagement of visual cortex posterior to somatosensory cortex. Such posterior rotating waves were also observed during spontaneous activity, particularly for waves with large radii (fig. S5A). These results demonstrate that substantial changes in rotating waves are associated specifically with correct performance of visual-motor associations.

Behavioral performance correlated with both arousal state and the phase of 2- to 8-Hz rotating wave band at stimulus onset. Miss trials were often preceded by a more prominent slow downward shift in visual cortex calcium activity, consistent with low arousal (fig. S15B).

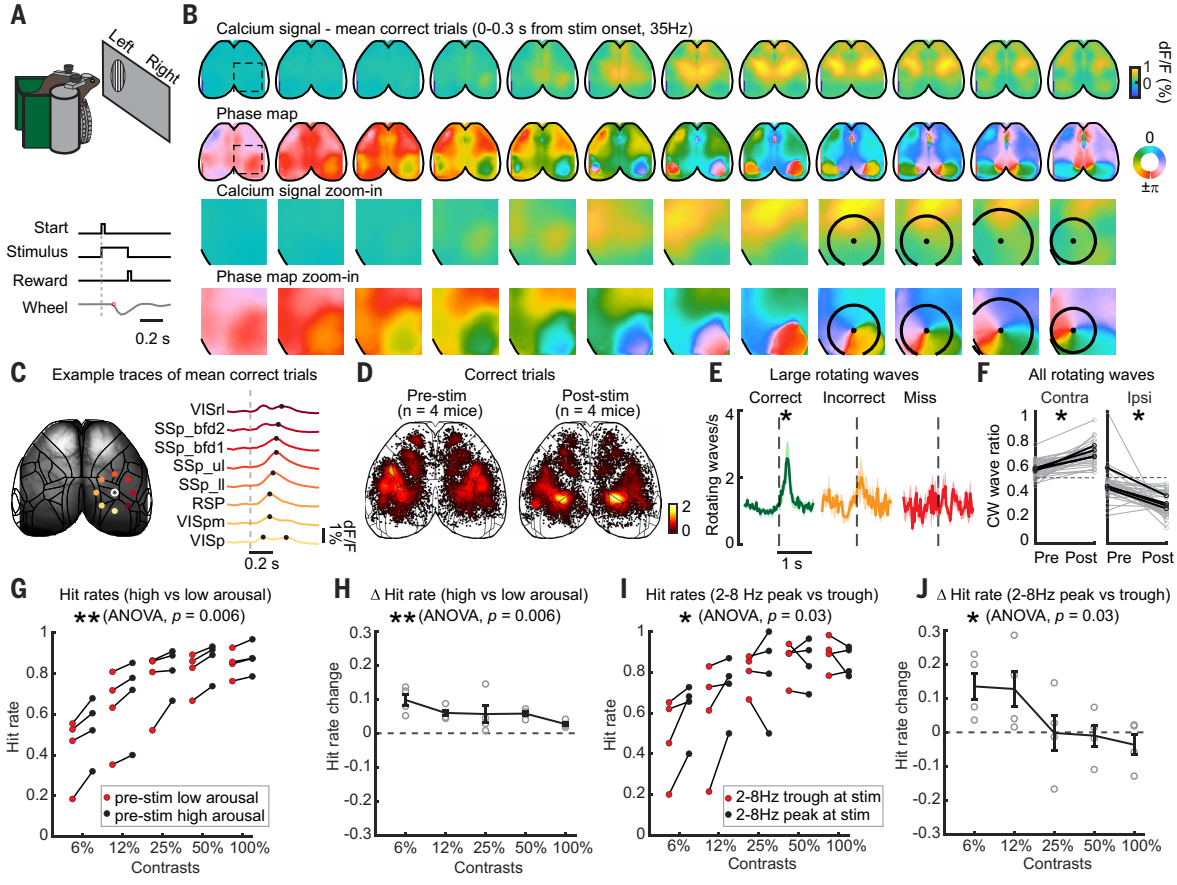

Fig. 6. Rotating waves during visual-motor behavior and their correlation with performance. (**A**) Schematic of the visual detection task. (**B**) Mean calcium activity and phase maps across the cortex aligned to stimulus onset in correct trials ($n = 4$ mice). Only correct trials with ≥25% contrast stimuli on the left screen are included. (**C**) Mean calcium activity traces from example sensory areas. Black dots indicate the times of local peaks in activity. (**D**) Spatial distribution of rotating waves at 200 ms before and after stimulus onset in correct trials ($n = 4$ mice). (**E**) Rates of large rotating waves (radius ≥1.73 mm) around stimulus onset for correct, incorrect, and miss trials. Data are shown as mean ± SEM, $n = 4$ mice. Significance was tested with within-subject session permutations and Bonferroni-Holm correction (see the Materials and methods). (**F**) Rotating wave directions before versus after stimulus onset in correct trials. Black lines indicate mouse averages; gray lines are session averages. (**G**) Hit rates (correct trials/total trials) split by prestimulus arousal state (high-arousal: 0.05- to 2-Hz power <25th percentile; low arousal: >75th percentile) and contrast ($n = 4$ mice). (**H**) As in (G) but showing hit rate change. (**I**) Within high-arousal states, hit rates split by 2- to 8-Hz phase at stimulus onset ($n = 4$ mice). (**J**) As in (I) but showing hit rate change.

Sorting trials by prestimulus low-frequency (0.05 to 2 Hz) power revealed significantly higher hit rates during high-arousal states than low-arousal states (Fig. 6, G and H; $P = 0.006$, two-way repeated-measures ANOVA). Prestimulus 2- to 8-Hz power did not correlate with hit rates overall. However, within high-arousal states, trials with a 2- to 8-Hz peak at stimulus onset had higher hit rates than those with a 2- to 8-Hz trough (Fig. 6, I and J; $P = 0.03$, two-way repeated-measures ANOVA), with the strongest effect observed under low-contrast conditions (fig. S15, C to G; 6 and 12%). These findings suggest that both arousal state and the phase of 2- to 8-Hz rotating waves at stimulus onset may contribute to perceptual performance.

Discussion

We observed frequently occurring rotating waves traveling across the somatotopic maps of the mouse sensorimotor cortex, matching a circular pattern of local axonal architecture. Rotating waves were also topographically mirrored between left and right cortical hemispheres, and between sensory and motor cortex, respecting long-range cortico-cortical connectivity. Rotating waves were widely distributed and coordinated across cortex, striatum, thalamus, and midbrain. Rotating waves occurred in diverse contexts: during high and low-arousal spontaneous states, during passive sensation, and during active behavior especially when performed correctly. These results establish that fast-traveling waves in the mouse brain are frequently organized as large-scale rotating waves, a pattern that is evident in a range of behavioral contexts. Moreover, they are not merely a local phenomenon but are globally coordinated across the brain, implying that the mechanisms of mesoscale spatiotemporal dynamics and their impacts on perception and behavior cannot be adequately understood by studying any one brain region in isolation.

Beyond the established modular and hierarchical sensory-processing pathways (*35*, *39*), we provide evidence that rotating waves propagate across primary sensory areas of different modalities with an underlying circular axonal connectivity. Rotating waves were centered in the middle of somatosensory cortex, an area of "unassigned" function in the Allen Common Coordinate Framework (CCF, "SSp-un") (*85*), unique in its poorly defined layer 4 compared with other somatosensory regions (*86*, *87*). Stimulation of a single sensory modality was sufficient to drive a rotating wave across somatosensory cortex, consistent with and expanding previous observations of wave propagation along barrel cortex rows (*88*–*90*). Previously reported crossmodal interactions (*36*–*39*) may reflect specific instances of a more general set of wave-based interactions.

Our findings demonstrate that rotating waves are simultaneously coordinated topographically across six cortical systems (left and right SSp, MOp, and MOs), refuting the notion that traveling waves can be adequately understood as arising within and affecting only a single brain region. Whereas local circular connectivity is consistent with the formation of rotating waves within somatosensory cortex, mirrored connectivity of long-range axonal projections is consistent with mirrored waves between hemispheres, as well as between sensory and motor cortex. Cortical rotating waves were causally dependent on the integrity of local circuitry within somatosensory cortex, although additional contributions from other systems cannot be ruled out.

We speculate that circular connectivity among cortical sensory systems may arise from repeated coactivation of neighboring peripheral sensors through plasticity mechanisms during development (*53*, *91*, *92*). Thalamic mechanisms may also contribute to global wave propagation (*57*, *93*–*97*). In particular, lateral connectivity within the reticular nucleus of thalamus or connectivity linking cortical regions through thalamic intermediaries might play a role in coordinating recurrent thalamocortical activity (*98*–*102*). The coupled oscillator framework could in principle be extended to incorporate subcortical structures for investigating how cortical-subcortical interactions shape rotating wave properties. Moreover, the presence of these waves in basal ganglia and midbrain, regions traditionally more tightly linked with motor function, raises the question of how these activity patterns interact with motor control and whether they extend to the pons, hindbrain, or spinal cord (*103*).

Spontaneous mesoscale dynamics encompass a rich repertoire of propagating and nonpropagating activity patterns spanning multiple spatial and temporal scales. Our findings establish rotating waves as a prominent motif of spontaneous and evoked spatiotemporal dynamics, with a defined morphological basis, brain-wide distribution, and behavioral relevance. How rotating waves interact with other spatiotemporal motifs to shape the variability of spontaneous activity remains an important open question. Our investigations were limited to a subset of frequency ranges and a single species. Whether dynamics beyond the frequency ranges we studied here (*12*, *16*, *17*, *22*, *104*) follow the same principles is an open question, because some evidence suggests that cortical activity in disparate frequency ranges may be uncoupled (*105*). Future studies incorporating voltage sensors may explore whether higher-frequency dynamics exhibit rotating waves at the spatial scales we studied (*106*). The high signal-to-noise ratio of the recent jGCaMP sensors we used was critical for detecting this detailed structure (fig. S4) and may explain why earlier studies did not systematically observe these patterns in spontaneous activity (*6*, *8*, *9*, *47*). The reduced rate of rotating waves during high arousal is consistent with either a genuine decrease of rotating wave rates or reduced detectability when 2- to 8-Hz power is low (*57*, *60*, *107*).

The rotating waves that we observed in mice have properties similar to those observed during human sleep spindles (*15*, *21*) and resemble in their directionality the traveling waves observed over small regions of human motor cortex (*108*), suggesting that these dynamics may generalize across species. Studies in nonhuman primates have identified traveling waves in a variety of contexts (*7*, Cat, not nonhuman primate, *12*, *14*, *22*, human study *29*–*31*), though with fields of view too small to meaningfully compare with the spatial structure that we observed. Thus, whether the global coordination of traveling waves occurs to the same degree in other species as in mice awaits further experimental confirmation (*109*–*112*).

What functions might these rotating wave dynamics serve? Rotating waves may act as spatiotemporal clocks, coordinating neuronal spiking to encode sequential sensation and action of the internal body, akin to hippocampal waves representing external space or events (*26*). During motor learning and execution, nearby body parts and their corresponding muscle groups are often activated sequentially (*92*, *113*). These waves could be involved in guiding plasticity mechanisms (*2*) to form connections between neighboring somatosensory and motor modalities, acting as functional highways for synaptic strengthening during sequential motor execution (*29*, *30*, *114*). During visual-motor tasks, large rotating waves were recruited specifically during correct trials, potentially conveying task-relevant signals across key areas. At the neuronal level, the identity of neurons that are modulated by these traveling waves (*115*), the nature of information borne on the waves, and whether neuronal participation dynamically changes with behavior and learning remain open questions. Rotating waves sweeping across topographic maps may provide the brain with an efficient mechanism for predicting natural sensory sequences and coordinating motor output. By imposing spatiotemporal structure on neural activity, these waves could supply contextual information for sensorimotor inference—analogous to the self-attention mechanism in transformer networks (*116*). This view is supported by computational models showing that spatiotemporally organized architectures with traveling waves efficiently encode and predict sequential data (*79*, *117*). Finally, these waves may form a "radar sweep" that sequentially scans modalities, modulating stimulus detectability in each region while maintaining metabolic efficiency

(*1*, *22*, *23*, *61*, *118*). Considered broadly, topographically coordinated rotating waves may provide the scaffold for a diverse array of perceptual and cognitive functions.

Materials and methods

Animals and virus injections

All experimental protocols were conducted according to US National Institutes of Health guidelines for animal research and approved by the Institutional Animal Care and Use Committee at the University of Washington.

The following transgenic mouse lines and viruses were used for this study (table S1). Mouse lines: (i) Ai210 (B6.Cg-*Igs7*$^{tm210(tetO\text{-}GCaMP7f;CAG\text{-}tTA2)Tasic}$/J, Jax, catalog no. 037378), dual-recombinase responsive (cre/flp-dependent), expressing tTA2 and jGCaMP7f; (ii) Ai195 (B6;129S6-*Igs7*$^{tm195(tetO\text{-}GCaMP7s;CAG\text{-}tTA2)Tasic}$/J, Jax, catalog no. 034112), dual-recombinase responsive (cre/flp-dependent), expressing tTA2 and jGCaMP7s; (iii) tetO-GCaMP8s (B6;D2-Tg(tetO-GCaMP8s)1Genie/J, Jax, catalog no. 037717), expressing jGCaMP8s, controlled by a tetracycline-responsive promoter element (TRE; tetO); (iv) Camk2a-tTA (B6.Cg-Tg(Camk2a-tTA)1Mmay/DboJ, Jax, catalog no. 007004), allowing the inducible expression of genes in forebrain neurons, when mated to strain carrying a gene of interest under the regulatory control of tetO; (v) Snap25-Cre (B6;129S-*Snap25*$^{tm2.1(cre)Hze}$/J, Jax, catalog no. 023525), knock-in mice with widespread Cre recombinase expression directed throughout the brain; (vi) VGlut1-FlpO (B6;129S6-*Slc17a7*$^{em1(flpo)Tasic}$/J, Jax, catalog no. 034422), knock-in mice with optimized FLP recombinase expression directed to VGlut1-expressing cells; (vii) VGlut1-Cre (B6;129S-*Slc17a7*$^{tm1.1(cre)Hze}$/J, Jax, catalog no. 023527), knock-in mice with Cre recombinase expression directed to VGlut1-expressing cells. Virus lines: (i) AAV-PHP.eB-syn-Flex-jGCaMP7s-WPRE (Addgene, catalog no. 104491-PHPeB), AAV PHP.eB particles produced from pGP-AAV-syn-FLEX-jGCaMP7s-WPRE (Addgene, catalog no. 104491) at titer $\geq 1\times10^{13}$ vg/ml; (ii) CAP-B10-soma-jGCaMP8m [gift from S. Grødem (*67*)], AAV with CNS- and neuronal-specific CAP-B10 serotype produced from pGP-AAV-syn-soma-jGCaMP8m-WPRE (Addgene, catalog no. 169257) at titer 3.5×10^{12} vg/ml; (iii) AAV-PHP.eB-hSyn-Cre (Addgene, catalog no. 105540-PHPeB), AAV PHP.eB particles produced from pENN.AAV.hSyn.HI.eGFP-Cre.WPRE.SV40 (Addgene, catalog no. 105540) at titer $\geq 1 \times 10^{13}$ vg/ml; (iv) AAV-PHP.eB-Syn-flpO-WPRE (gift from T. Daigle, Allen Institute for Brain Science), AAV PHP.eB particles were produced from Syn-FlpO-WPRE at titer 4.1×10^{13} vg/ml.

We used five different strategies to express jGCaMP7/8 across the brain: (i) Ai210 or Ai195 mice were bred with Snap25-Cre or VGlut1-FlpO, then injected with AAV-PHP.eB-Syn-FlpO or AAV-PHP.eB-hSyn-Cre virus (3-5 μl) retro-orbitally in 4-6 week-old mice for dual cre/FlpO-dependent jGCaMP7f or jGCaMP7s expression throughout the brain; (ii) Ai210 mice were bred with Snap25-Cre positive and VGlut1-FlpO positive mice, to create triple transgenic mice that expressed jGCaMP7f in excitatory neurons throughout the brain; (iii) Retro-orbital injection of CAP-B10-soma-jGCaMP8m (100 μl) in 4- to 6-week-old wild-type mice; (iv) Retro-orbital injection of AAV-PHP.eB-flex-GCaMP7s (40 μl) in 4- to 6-week-old VGlut1-Cre mice; and (v) tetO-GCaMP8s mice were bred with Camk2a-tTA mice.

In total, 32 mice of both sexes with GCaMP expression were used (table S1), mostly between 2 to 8 months old (median at 4 months old) when the first experiment was conducted. 15 mice were used for wide-field imaging only experiments during spontaneous behavior, 19 mice (32 sessions) were used for simultaneous wide-field and electrophysiological recordings. $n = 5$ mice (one session for each mouse) were used for passive whisker pad stimulation experiments, $n = 4$ mice (35 sessions) were used for wide-field during visuomotor behavior experiments, and $n = 5$ mice were used for cutting experiments. Some mice were used for multiple different experiments. Our findings were consistent across different expression strategies, and therefore we combined these mice in the analysis unless specified.

Surgery

The surgical preparation was similar to that used previously for whole-cortex wide-field imaging (*119*). Mice were anesthetized under 3 to 4% isoflurane in an induction chamber first, then maintained at 1 to 2% isoflurane for the duration of the 1- to 2-hour procedure. Carprofen (5 mg/kg) was administered subcutaneously and lidocaine (2 mg/kg) was injected under the scalp for postoperative analgesia. The scalp was shaved and further cleaned with hair removal cream before mice were transferred to a separate stereotaxic frame for surgery. Eye ointment (Alcon, Systane) was applied before surgery to prevent drying and body temperature was kept at 37°C with a far infrared warming pad (Kent Scientific). The skin and periosteum connective tissue was cleared off the dorsal surface of the skull. A layer of cyanoacrylate (Vetbond Tissue Adhesive) was then applied to seal the junction between the exposed skull and cut skin. A 3D-printed plastic recording chamber was implanted on top of the skull with dental cement (C&B Metabond) to provide light isolation during experiments, and a custom-made steel headplate was attached to the skull over the interparietal bone with Metabond for head fixation. To create a clear coating suitable for imaging, we consecutively applied two separate thin layers of fast curing optical adhesive (NOA81, Thorlabs) and cured until solidification with a 365 nm, 3 W output power UV Flashlight (LIGHTFE, UV301D). Carprofen (0.05 mg/ml) was given for 3 days in water after surgery. Mice were allowed to recover in the home cage for at least 5 days before habituation to head fixation.

Wide-field imaging and data processing

The wide-field imaging setup was custom-built with a macroscope body (sciMedia fluorescent beam splitter DLFLSP2R) fitted with a CMOS camera with 3.45 μm/pixel resolution (Basler ace acA2440-75 m) and a 0.63× objective lens (Leica Planapo 0.63×). Alternating dual light illumination was generated using an OptoLED system (Cairn Research) with blue (470 nm) and violet (405 nm) LEDs to capture GCaMP calcium signal and hemodynamic intrinsic signal at 35 Hz each, respectively. Images were captured at 70 Hz using external triggers synchronized to the light illumination and binned at 3×3 pixels to increase signal-to-noise ratio and reduce data size. This results in a final resolution of 17.3 μm/pixel for the collected imaging data. To reduce light artifacts for Neuropixels recordings during imaging, the LED onset and offset were modified to be a 3-ms sine-wave ramp by controlling the analog voltage output from a microcontroller board (Teensy 3.2), resulting in an effective 11-ms exposure time at full intensity for each frame.

For wide-field imaging experiments, mice were acclimated to head-fixation for at least two sessions before recording, after recovery from headplate implant surgery. Head-fixed mice were seated on a plastic tube with forepaws on a left-right rotating rubber wheel (*83*). For wide-field imaging experiments during spontaneous activity, 11/15 mice were water-restricted with intermittent passive water reward, and 4/15 mice were in resting states without water restriction. In water-restricted sessions, two 20-min passive water-reward blocks were interleaved with one or two 20-min resting-state blocks. During passive water-reward blocks, a drop of 2 to 3 μl of water was automatically dispensed through a TTL-controlled pinch valve (Clippard, NPV2-1C-02-12; CoolDrive, 161D1X250) every 10 to 15 s to promote alertness. Total recording time across sessions ranged from 40 to 80 min. Because no significant differences were observed in rotating wave distributions across conditions, all sessions were included for analysis. Seven of 15 mice had simultaneous face and pupil tracking. Three iPad screens were positioned around the mouse at right angles. A 3D-printed cone was designed to connect the recording chamber with the macroscope objective to shield the subject's eyes from the LEDs and prevent light contamination of the imaging signal. Eye position and facial movements were tracked simultaneously with separate infrared cameras (eye position: Navitar Zoom 7000; facial movement: FLIR Chameleon3) with external infrared illumination (CMVision IR30, 850 nm). Cortical visual areas were mapped using white visual sparse

noise squares asynchronously on a black background and visual field sign maps (fig. S4) were computed as in Peters *et al.* (*48*).

For wide-field data analysis, non-neuronal signals arising from changes in blood flow were removed by subtracting the violet-light evoked signals from the blue-light evoked signals with linear regression, which resulted in an effective sampling rate of GCaMP activity at 35 Hz (*110*, *119*, *120*). In brief, a scaling factor was first fit for each pixel between two signals that were band-pass filtered in the range of 10 to 13 Hz (heartbeat frequency, with largest hemodynamic effect expected). The hemodynamic-corrected traces were therefore the blue traces in full frequency range subtracted by the scaled violet traces (*48*, *119*). All wide-field data were aligned to the Allen CCF (*85*) with affine transformation using four anatomical landmarks as in Musall *et al.* (2019) (*110*), which were the left, center and right points where the anterior cortex meets the olfactory bulbs, and the medial point at the base of retrosplenial cortex. Alignment results were further verified with retinotopic visual field sign maps, with visual fields aligned within the boundaries of the visual CCF coordinates (fig. S4).

To store and process the data effectively, we compressed the wide-field data (D) into spatial components (U) and temporal components ($S*V$) with singular value decomposition in the form $D = USV^T$, as previously described (*48*, *61*). We used the top 50 singular vectors, which accounted for 97.3 ± 0.5% (mean ± SEM, 15 mice) of total variance before compression. Finally, we took the temporal derivative of the signal, which better reflects the underlying spiking activity, acting as an approximate deconvolution (*119*). We describe the data after these steps as "raw" data in Fig. 1 and elsewhere, unless specified, because it has not undergone bandpass filtering. We divided the wide-field signal by the average fluorescence at each pixel, to get $\Delta F/F$ normalized signal.

Simultaneous Neuropixels recording and wide-field imaging

For sessions combining wide-field imaging and Neuropixels recordings, 18/32 sessions were water restricted with interleaved licking blocks, whereas 14/32 sessions were in resting state. Penetration angles and positions of four-shank Neuropixels 2.0 probes (*121*) for subcortical recordings were carefully designed to maximize the coverage of sensory modalities in each subcortical region (thalamus, striatum and midbrain) based on the 3D axonal projection maps from the Allen Mouse Brain Connectivity Atlas (*46*), using the neuropixels trajectory explorer (https://github.com/petersaj/neuropixels_trajectory_explorer) and Pinpoint software (*122*). In detail, eight injection experiments with anterograde virus injection sites at VISp [ID: 309003780], RSP [ID: 166054929], SSp-tr [ID: 100141495], SSp-ul [ID: 286312782], SSp-ll [ID: 272698650], SSp-m [ID: 157654817], SSp-n [ID: 168163498], SSp-bfd [ID: 127866392] were selected and 3D projection density volumes were downloaded from the Allen Mouse Brain Connectivity Atlas. Intensity-weighted centers of the eight projections within each subcortical region (thalamus, striatum and midbrain) were identified, and a 2D plane was fitted from these center points. Optimal angles and depths of the four-shank probe were then selected within the fitted 2D plane, which covered most of the projected center points (table S2).

Before moving the four-shank probes with the angle and depth parameters below, the 2D face of the four-shank probe was positioned perpendicular to the AP (anterior-posterior) axis of the brain and above the right hemisphere of the brain. All angle and depth parameters were measured for the first shank that was closest to the sagittal suture. For striatal recordings, we used two angle strategies, (1) from the method described above and (2) parameters from Peters *et al.* (*48*), where the authors mapped cortical-striatal functional correspondence. AP coordinates were referenced to the bregma position, medial-lateral (ML) coordinates were referenced to the sagittal suture, azimuth angles were counterclockwise rotation around the dorsal-ventral (DV) axis from the dorsal-to-ventral view, elevation angles were clockwise rotation around the AP axis from the posterior-to-anterior view, spin angles were counterclockwise rotation around the probe axis from the probe base-to-tip view.

On or before the first day of recording, a 1- to 2-mm-diameter craniotomy was prepared with a dental drill over the target brain area under anesthesia, leaving the dura intact. The craniotomy was protected with transparent dura-gel (Dow Corning 3-4680 silicone gel), with a further 3D-printed protective cap sitting on top of the recording chamber. After several hours of recovery, mice were head-fixed in the recording setup. A light shield cone was installed to connect between the recording chamber and the top edges of the iPad screens to block imaging light from the mouse's eyes while achieving maximum probe angle flexibility. We used internal reference configuration for all recordings, with ground and reference connected. In detail, a probe was directly inserted through the dura gel without solution bath and the reference site on the probe tip was used for grounding and referencing. Before each insertion, the electrode shanks were coated with CM-Dil (Invitrogen), a red lipophilic dye, for later histological reconstruction of probe tracks.

Histology

To recover electrode tracks, the brain tissue was first extracted after perfusion with 4% formaldehyde under terminal anesthesia, followed by tissue clearance with the iDISCO protocol (*123*). Image stacks of the brain sample were acquired with a light-sheet microscope (LaVision Biotec UltraScope II) at 561 nm excitation channel for DiI and 488 nm for autofluorescence. The 3D sample volume was then registered to Allen CCF (*85*) using open source package 'ara_tools' based on image registration suite Elastix (https://github.com/SainsburyWellcomeCentre/ara_tools). The electrode tracks were manually traced within the 3D sample volume space using open source package 'lasagna' (https://github.com/SainsburyWellcomeCentre/lasagna).

Power spectrum analysis (fig. S1)

To compute the power and power ratio map in the 2- to 8-Hz frequency band across the cortex efficiently, we computed the power spectrum on the temporal components of the data ($S*V$) after singular value decomposition, and transformed the power spectrum back to the 2D space by multiplying the spatial components (U) (*61*). Power spectrum was performed using multitaper fourier transform (*124*) and averaged across multiple 20-s epochs of data. Power spectrums across mice were averaged to construct a 2- to 8-Hz "power map" across the cortical pixels (fig. S1C). We also used a fast Fourier transform approach to construct the 2- to 8-Hz "power map" and achieved the same results (data not shown). Example power spectrums were constructed with the original data without taking the derivatives (Fig. 1 and fig. S1D).

Rotating wave detection and quantification (Fig. 1 and figs. S1 to S8)

Rotating wave detection algorithm (Fig. 1 and figs. S1 and S2): To capture the dynamics of the wide-field time series data, we first took the first-order derivative of the calcium traces, approximating a deconvolution to better match underlying firing rates (*119*), and then filtered the traces with a second-order Butterworth bandpass filter at 2- to 8-Hz with zero phase distortion. To extract the spatial distribution of the oscillation phase angle over time, the Hilbert transform is applied after filtering to each pixel independently. The algorithm we used was the standard Hilbert transform based on the fast fourier transform (*hilbert* in Matlab), where the angle of the analytic signal after Hilbert transform is the instantaneous phase. For visualization, the phase information for all pixels was plotted together to construct phase maps over time (Fig. 1, A and B, and fig. S2).

To automatically detect rotating waves (fig. S2), we took advantage of the fact that phase angles along the rotating wave circle for any given radius cumulatively increase by 2π. We designed a three-step algorithm with a coarse-to-fine approach to identify rotating wave centers and radii. Step 1: Coarse grid search for rotating waves. Each

frame is zero padded with 120 extra pixels (2 mm) on each of the four edges first to effectively detect rotating waves near the edge or with large radii. Rotating waves were first identified on a coarse grid (10 × 10 pixels, 173 x173 μm spacing). Because the phase angle distribution within a rotating wave is noisy at times, we defined two broad criteria for rotating wave detection: (1) angular differences of 10 evenly sampled points along the rotating wave circle cumulatively added up to near $\pm 2\pi$ ($2\pi \pm 0.32\pi$), with opposite signs representing clockwise and counterclockwise rotating wave directions; (2) at least one out of the 10 points sampled lies in each of the 4 quadrants within 0 to 2π range. At each search grid, 3 small circles (radii at 10, 15, and 20 pixels, which are 173, 260, and 346 μm) were sampled independently. If at least two of three sampled circles passed the two criteria above, then the grid coordinate was considered a candidate rotating wave position. Step 2: Clustering nearby candidate rotating wave centers. A robust rotating wave was often detected at multiple nearby candidate grid points. Rotating wave centers separated by a Euclidean distance less than 15 pixels (260 μm) were grouped together, and the mean coordinate of the group was taken as the intermediate candidate rotating wave center. Step 3: Refined rotating wave search and radius determination. The final positions of rotating waves were refined with the same algorithm from step 1 and 2 within a 20 × 20 pixel region of interest (ROI) at full resolution based on the intermediate candidate rotating wave coordinates from step 2 through a pixel-by-pixel search. The final radius was tested from 10 to 100 pixel values at 10 pixel steps (from 173 μm to 1.73 mm, at 173 μm steps), and the maximum radius was identified as the largest radius for which the two criteria in Step 1 were satisfied.

Phase randomization control for rotating wave occurrence (fig. S3): Rotating waves can randomly occur within spatially and temporally smooth dynamics. To ensure that the rotating waves we observed were not by chance, we constructed surrogate data using a Fourier-based phase randomization, which preserved both the spatial and temporal correlations of the raw data (*17*, *65*). We performed the fast Fourier transform on the 3D raw data (x, y, t), randomized the phase values of the Fourier components by shuffling the index of the 3D phase matrix, and then reconstructed surrogate data with the inverse Fourier transform. To avoid including areas outside of the brain in the anterior space for the Fourier transform, we drew a rectangle in the posterior cortex and used only this area for both raw data and surrogate data comparison. We then applied the rotating wave detection algorithm to the raw data and surrogate data within the rectangle region, and compared distributions of detected rotating waves (fig. S3). Peak rotating wave density for rotating waves with radius greater than or equal to 0.69 mm within the somatosensory cortex (SSp) were significantly higher in the real data than in the surrogate data across 15 mice tested (fig. S3). Therefore, we only included rotating waves that had radius greater than or equal to 0.69 mm for further analysis.

Rotating wave sequences and permutation control (Fig. 1): To group traveling rotating waves into spatiotemporally connected rotating wave sequences, we classified rotating waves that were less than 30 pixels (0.5 mm) apart in Euclidean distance in neighboring frames to be in the same sequence group (Fig. 1D). To determine whether the rotating wave sequences we observed could arise from chance with the same overall rate of rotating wave occurrence, we permuted the frame identity for all included rotating waves (those with radius greater than or equal to 0.69 mm) within a session 1000 times and recomputed the sequence grouping. Proportions of rotating waves that belonged to a sequence with duration lasting for more than one frame (29 ms) were consistently and significantly lower in the permutations compared with our observed data ($P < 1 \times 10^{-7}$, unbalanced two-way anova; Fig. 1D), whereas the proportion of single-frame rotating waves in the permuted distribution was significantly higher than in observed data ($P < 1 \times 10^{-7}$, Student's t test; Fig. 1D). We therefore excluded single-frame rotating waves from further analysis. Nevertheless, single-frame rotating waves (29 ms) were also spatially concentrated within the SSp center (fig. S5).

Rotating wave center density estimation (Fig. 1 and figs. S4 and S5): To estimate the spatial density of rotating wave centers in cortex, we drew a local square (0.4*0.4 mm^2) around each unique rotating wave and counted total rotating wave centers within the square. All rotating waves (with radius greater than or equal to 0.69 mm) that were within a rotating wave sequence (≥2 frames) were included for the rotating wave center density plot. Given total frame numbers within a session and the sampling frequency of 35 Hz, we then converted these counts to density rates with units of rotating wave centers/mm^2/s. For the summary rotating wave density plot (Fig. 1E), all 15 sessions were concatenated for rotating wave density estimation.

Rotating wave symmetry quantification (Fig. 3 and fig. S6): Three peaks in the rotating wave center density plot were observed on each hemisphere, centered on SSp, MOp and MOs respectively (Fig. 1 and fig. S6, C and D). To determine whether rotating waves are symmetrical and therefore are traveling in opposite directions in neighboring structures, we grouped all detected rotating waves into 6 regions for quantification: SSp, MOp and MOs regions in the left and right hemisphere. The borders between regions were based on Allen CCF (*85*) after alignment in the Materials and methods section "Wide-field imaging and data processing." We compared rotating wave directions between MOp and SSp within each hemisphere (left MOp-SSp, right MOp-SSp), MOp and MOs within each hemisphere (left MOp-MOs, right MOp-MOs), and between each of the three regions across hemispheres (SSp left-right, MOp left-right, MOs left-right). When a pair of rotating waves were detected simultaneously in a single frame in both neighboring regions, the directions of the rotating waves were compared. When the two neighboring rotating waves were traveling in opposite directions, they were considered to be matched (fig. S6F), in the sense that our hypothesis based on the mirrored topographic organization of these regions (*41*) predicted mirrored dynamics.

Rotating wave modulation across arousal cycle of behavior (Fig. 1 and fig. S6): Pupil and face motion videos were captured at 70 Hz with the same digital triggers as the wide-field camera. Pupil fluctuations and lick positions were tracked using DeepLabCut (DLC) (*125*). Pupil diameter traces were smoothed with a 1-s median filter. Facial motion energy for each frame was calculated as the sum of the absolute intensity difference across pixels between consecutive frames, with higher values reflecting greater movement. Lick times were extracted from the DLC tongue position trace using a peak detection algorithm in Matlab. The 2- to 8-Hz amplitude was estimated as the mean instantaneous amplitude through Hilbert transform across seven selected pixels within the sensory cortex (Fig. 1A). In the example shown (Fig. 1I), rotating wave rates and 2- to 8-Hz amplitudes were smoothed in a 1-s time window for visualization.

Magnitude-squared coherences between neural activity and behavioral fluctuations (pupil or face motion) across frequencies were computed using *mscohere* function in Matlab with a 4096-sample (117 s) Hamming window and 50% overlap. Phase differences between two signals across frequencies were derived from the complex angles of the cross power spectral density (*cpsd*) function in Matlab. Coherence at a given frequency was considered significant if the mean-SEM value at that frequency exceeded the 95th-percentile surrogate threshold. Surrogates were generated by Fourier-based phase randomization of the behavioral time series (pupil or face motion), preserving the power spectrum while randomizing phase. This permutation was repeated 500 times, and the resulting coherence distributions were concatenated across sessions to obtain the 95th-percentile threshold for each frequency. Notably, the frequency range showing significant coherence

closely matched the frequency range with consistent phase differences (fig. S6, G and H), validating the thresholding approach.

The phase-amplitude relationship between the phase of behavior fluctuation (0.05 to 0.5 Hz), and 2- to 8-Hz amplitudes of neural data were calculated by binning the 2- to 8-Hz amplitudes into 18 phase bins of the behavior fluctuation (from −π to π). To highlight the circular-linear relationship across sessions, amplitudes were mean-subtracted per session, yielding zero-centered values. Similarly, the phase-wave rate relationship between the phases of behavior fluctuation (0.05 to 0.5 Hz) and rotating wave rates was calculated by sorting detected rotating wave centers into 18 behavioral phase bins (from −π to π). Peak density of rotating waves was then calculated for each phase bin.

Synchrony index, rotation index and plane wave index (fig. S7): To quantify traveling waves across all frames, we designed a synchrony index and a rotation index (fig. S7, A to D). Synchrony index (R_{sync}) is the mean resultant vector length of all phase angles in a frame (length of the vector sum/total length):

$$R_{\text{sync}} = \frac{\left|\sum_{x=1}^{m}\sum_{y=1}^{n} e^{i\cdot\alpha_{xy}}\right|}{m \times n}$$

where $\alpha_{x,y}$ is the phase angle of the [x, y]-th pixel within a frame of frame size [m, n]. Each phase angle is represented as a vector with unit length of 1, resulting in a total length equal to the number of pixels in the frame ($m \times n$). Synchrony index (R_{sync}) is bounded between 0 and 1. Synchrony index close to 0 indicates all phase angles are random, and synchrony index close to 1 indicates all phase angles are uniform.

However, the synchrony index does not differentiate rotating wave patterns from randomness. The synchrony index for rotating wave–like patterns is also close to 0, because all phases with opposing directions are represented in a rotating wave. Therefore we designed a rotation index (R_{rotation}), to quantify how close the phase map (A) from a single half-hemisphere of size [m, $n/2$] from a sampled frame with size [m, n], matched to a perfect rotating wave template (B) of the same size ([m, $n/2$]; fig. S7, B and D). Angles (β) within the rotating wave template (B) were constructed with a four-quadrant inverse tangent function of the position matrix [u_x, v_y], which were bound in the closed interval [−π, π]:

$$\beta_{x,y} = a\tan 2\left(v_y, u_x\right), \text{where } u_x \in \left[\frac{-m}{2}, \frac{m}{2}\right], v_y \in \left[\frac{-n}{4}, \frac{n}{4}\right]$$

Rotation index (R_{rotation}) is the mean resultant vector of the angular difference map (θ):

$$R_{\text{rotation}} = \frac{\left|\sum_{x=1}^{m}\sum_{y=1}^{n/2} e^{i\cdot\theta_{xy}}\right|}{m \times n/2},$$

$$\theta_{x,y} = \alpha_{x,y} - \beta_{x,y}$$

where θ is the angular difference between phase angles (α) in a sampled half-hemisphere frame (A) with [m, $n/2$] size and a rotating wave phase template (β) with a perfect rotating wave (B) of the same size. 0 indicates no rotating-wave-like features in the frame, and 1 indicates a rotating-wave-like frame.

Sum index (S) is defined as:

$$S = \sqrt{{R_{\text{sync}}}^2 + {R_{\text{rotation}}}^2}$$

which is also bounded between 0 and 1, as frames with high synchrony index have low rotation index and vice versa (fig. S7F).

To systematically quantify plane waves (fig. S7, P and Q), we first calculated the cortical flow vector field using phase maps from consecutive frames within the 2- to 8-Hz range, as described in the Materials and methods section "Traveling wave quantification with optical flow." We then used an order parameter, the plane wave index, to measure the coherence of the plane wave in each frame (*7*, *66*). This index is defined as the average normalized vector field velocity (φ):

$$\varphi(t) = \frac{\left|\sum_{x,y} w(x,y,t)\right|}{\sum_{x,y}|w(x,y,t)|}$$

where $w(x, y, t)$ is the flow vector field at position (x, y) in the frame at time t. Therefore, φ(t) is the absolute length of summed vector fields normalized to total absolute vector length at time t. The plane wave index is bounded between 0 and 1, with values close to 1 indicating coherent motion of all flow vectors and values close to 0 indicating random motion. We used a threshold of 0.6 to identify frames with significant plane wave activity, similar to thresholds applied in previous studies (*7*, *66*).

Rotating wave speed (Fig. 1 and fig. S8): We calculated optical flow from sequential pairs of phase-map frames with the Horn-Schunck method (*7*, *126*) to illustrate directions of wave travel (Fig. 1C). To quantify rotating wave speed accurately (fig. S8), we sampled 12 evenly spaced points on circles of varying distance from the rotating wave center within each detected rotating wave. We used all rotating waves within a 1.7 × 3.4 mm square centered on SSp in the right hemisphere across all mice (Fig. 1, F and G, and fig. S8). Angular speed (ω, rad/s) for any point within the rotating wave was calculated with the following equation:

$$\omega = \text{angle}\left(e^{i\cdot(\theta 1 - \theta 2)}\right) \times f$$

where θ1 is the phase angle for the sampled point of current frame, θ2 is the phase angle for the sampled point of the next frame, f is the sampling frequency (35 Hz). Angular difference is wrapped in the interval [−π, π] with Euler's formula and angle function in matlab.

We then calculate linear speed (v):

$$v = r \times \omega$$

where r is the distance of the sampled point to the rotating wave center, ω is the angular speed for the sample point.

Single-neuron axonal arbor analysis (Fig. 2 and fig. S9)

To investigate the morphological basis of rotating waves in the cortex, we used the Single Neuron Reconstruction Dataset (*72*), in which 1741 neurons from various brain regions were sparsely labeled and reconstructed after whole-brain imaging. Out of 1741 neurons throughout the entire brain, 435 neurons were labeled within the left sensory cortex. We analyzed 120 neurons within the motor cortex on the same left hemisphere separately with the same methodology (fig. S9, A to D). The sensory cortex includes visual cortex (VIS), auditory cortex (AUD), retrosplenial cortex (RSP), primary somatosensory cortex (SSp) and secondary somatosensory cortex (SSs). To reveal the local axon architecture within the sensory cortex, we excluded long-range axon projections, i.e., projections to the subcortical areas, to the contralateral hemispheres, and to motor areas of cortex. For SSs and AUD, where ipsilateral long-range projections were prevalent, only axons restricted to the local regions (SSs and AUD only) were analyzed. The singular value decomposition was computed for each neuron's 2D point cloud (in the AP-ML plane) of axon terminals (ending points of axon branches). The first singular vector was taken as the dominant direction of the axonal arbor. A "polarity index" was computed to capture the elongation of the axonal arbor

$$P = \frac{s_1}{s_2} - 1$$

where P is the polarity index, s_1 is the first singular value, and s_2 is the second singular value. A polarity index closer to 0 indicates symmetrical distribution of axon terminals on the first two major axes, and

larger values indicate a dominant distribution of axon terminals on the first major axis.

Axon-to-SSp-center angle (θ) is calculated as the angle between (1) the axonal first singular vector (s_1) and (2) the vector from the SSp center to cell soma. The permuted distribution is generated by scrambling the soma position of each neuron 100 times while preserving the direction of the singular vector, and recalculating the SSp-center bias.

To compare axon orientations to rotating waves in the mesoscale activity, we computed a mean rotating wave flow field by averaging the optical flow across all rotating waves with a large radius around the SSp center that were counterclockwise traveling in one hemisphere in all 15 mice used. We then sampled flow vectors within the flow field at the soma positions of all 435 sensory neurons used in the axon vector map (u), forming a paired flow vector map (v). We then designed an axon-flow field vector matching index, which is the sum of absolute values of the dot product of all axon vectors (u) and flow field vectors (v) at the same soma location, normalized by the sum of dot products of vector length:

$$\text{index} = \frac{\Sigma_{i=1}^{n}\left|\text{dot}(u_i, v_i)\right|}{\Sigma_{i=1}^{n}\left(|u_i| * |v_i|\right)}$$

If angles between two vectors at the same soma location are ±90°, then the dot product is zero; if they are matching either at 0° or 180°, the absolute value of the dot product is maximized. As a result, an index of 1 indicates perfect matching of all axon and flow vectors, and an index of 0 indicates total randomness. Axon vector length is the polarity index (P) of the neuron. The null hypothesis that axon polarity is unrelated to activity flow vectors was tested by permuting the flow vectors, that is, assigning each of the 435 spatial coordinates to have a flow vector randomly drawn without replacement from the set of all 435 flow vectors in the original map. The null distribution was generated by permuting the flow vector map 1000 times and recalculating the matching index.

Coupled oscillators with circular connectivity bias and mirror symmetry (Fig. 2 and fig. S10)

Coupled oscillator model with Kuramoto equation: To capture rotating waves mathematically, we built a minimal model of spatially-coupled phase oscillators which could be naturally extended to include circular connectivity bias (*75*, *127*). The rate of phase change for the i-th oscillator ($\frac{d\phi_i}{dt}$) in a system composed of N oscillators is following the Kuramoto equation (*75*–*77*):

$$\frac{d\phi_i}{dt} = \Omega + K\sum_{j=1}^{N} W_{ij}\sin(\phi_j - \phi_i) + u_i I(t)$$

Each oscillator has an intrinsic natural frequency at Ω, and is coupled to all other oscillators with coupling weights W_{ij}. The interactions between two oscillators depend sinusoidally on the phase difference between them. K is the global coupling weight scale. The correlated noise term $u_i I(t)$ models global environmental fluctuation, which is composed of a fixed noise term per oscillator u_i with ~N(0,1) normal distribution multiplied by a time-varying noise signal $I(t)$ with standard deviation controlled by the noise scale parameter ~N(0, noise_scale) affecting all oscillators.

We begin by generating a point set in 2D space, with oscillators positioned on an evenly spaced Euclidean grid (50 by 50 grid size) within a circular boundary (maximum radius at 1), which resulted in ~N = 1876 oscillators. Natural frequencies (Ω) were drawn from a Gaussian distribution with mean frequency at 5 Hz and standard deviation at 0.5 Hz. The initial phase values were randomly distributed uniformly between 0 and 2π. Simulations were integrated using Euler method with time step dt = 0.01 for a total duration of T = 50 time units (total 5000 time steps). Coupling weights W_{ij} were generated differently in isotropic and circular bias models, as described below. We focus on the distance-dependent connectivity as the main factor for model comparison without adding axonal conduction delay, because both local (2 to 5 ms) and long range (8 to 20 ms) conduction delays are relatively short compared with the slow temporal scale of rotating waves (2 to 8 Hz, 125 to 500 ms/cycle). Future work incorporating conduction delay could further constrain wave dynamics in both circular biased model and mirrored-connectivity model.

Isotropic model: In the isotropic model, connectivity between oscillators was determined based on Euclidean distance in Cartesian coordinates (x, y). We used a simple connectivity rule. If the Euclidean distance between two oscillators i and j was within a coupling radius (r_{coupling}) of 0.4, then there was 25% probability (p_{coupling}) that the coupling weight between them (W_{ij}) is 1, otherwise 0. The Euclidean distance between two oscillators (x_i, y_i) and (x_j, y_j) were computed as

$$d_{ij} = \sqrt{(x_i - x_j)^2 + (y_i - y_j)^2}$$

Connection weights for each oscillator were then normalized by its total weights, so that total synaptic input strength for each oscillator was balanced. This isotropic connectivity model produced a sparse but well-connected network, with no preferential connectivity direction.

Circular bias model: The circular bias model incorporates the circular connectivity constraint by computing connectivity weights between two points in polar coordinates (θ, r), where θ represents the angular position and r represents the radial position from the center. We used the same 1876 point sets in 2D space as in the isotropic model. However, the distance between two oscillators (θ_i, r_i) and (θ_j, r_j) was computed as

$$d_{ij} = \sqrt{\beta(\Delta\theta_{ij})^2 + (\Delta r_{ij})^2}$$

Where $\Delta\theta_{ij} = \min\left(\left|\theta_i - \theta_j\right|,\ 2\pi - \left|\theta_i - \theta_j\right|\right)$ accounts for the periodic angular boundary conditions in the angular direction so that points nearby 360° in angle were treated as neighbors, $\Delta r_{ij} = \left|r_i - r_j\right|$, and β is a tunable parameter to adjust the relative contributions of tangential versus radial distance to connectivity strength. Strengthened rotating wave dynamics occur consistently when β = 1 (equal contributions) or β = 0.5 (stronger tangential contribution), and we used β = 1 for all subsequent analyses. The same coupling radius (r_{coupling} = 0.4) and coupling probability (p_{coupling} = 25%) were used to generate circular bias connectivity maps.

We constructed our circular bias model by incorporating a feature of the morphological observation to the model (Fig. 2, G and H): axonal length of individual neurons increases with soma distance from the SSp center, meaning that neurons in the outer radius have a higher probability of forming connections in the tangential axis despite greater separation distances. We implemented this feature by constructing the connectivity map in polar coordinates, which creates uniform connectivity strength/probability across both radial and angular directions in polar coordinates. Thus, two oscillators separated by the same angle have equal connectivity regardless of whether they are near the center or at the edge of the domain (fig. S10, A and B). Because arc length increases with radius for a fixed angle, this creates stronger effective connectivity in the tangential direction for oscillators at larger radii when viewed in Cartesian space, whereas radial connectivity strength remained uniform across all radii (Fig. 2I). A rotating wave in Cartesian coordinates is equivalent to a plane wave in polar coordinates. An intuitive explanation of stabilized rotating wave patterns in the circular bias model is that propagating waves preferentially form along the longer dimension of a 2D sheet. In polar coordinates, the circular direction (circumference = 2π*radius) is longer than the radial direction (r), favoring wave propagation tangentially rather than radially (fig. S10, A and B).

Rotation index: We sought to characterize the presence of rotating waves in the baseline isotropic model and circular bias model for topographically coupled oscillators (Fig. 2, I and J, and fig. S10, D and E). As a complementary tool to study the presence of rotating waves, we leveraged a population scale metric related to synchronization to look for the presence or absence of rotation (*Sp*), which measures how closely a phase map matches a perfectly centered rotating wave. This is the same as the definition of rotation index (R_{rotation}) as described in the Materials and methods section "Synchrony and rotation index" (fig. S7):

$$Sp(t) = \left(\frac{1}{N}\right) \times \sum_{j=1}^{N} e^{i(\phi_j(t) - a\tan2(y_i/x_i))}$$

where $Sp(t)$ is the rotation index at time t, $[x_j, y_j]$ is the position index for the j-th node in the 2D random point set, $\phi_j(t)$ is the phase value of the j-th node at time t of simulation, $a\tan2(y_j/x_j)$ is the phase value of the j-th node of the center rotating wave template, and N is the total number of nodes in the 2D random point set.

Rotation index (*Sp*) measures how close the current configuration is to the perfect rotating wave configuration centered at the center of the field of view on a scale of 0 to 1, with 1 only being achieved when the full field is a rotating wave centered in the field of view. Equipped with this tool, we sought to characterize rotating waves in our baseline model. Across 25 random seeds, we found that rotating waves were more likely near the transition between a desynchronized regime and a synchronized regime. In the crossover vicinity (near a critical line in the space of noise and coupling scale, separating these two regimes), we observed a substantial uptick in the rotation index of these fields (Fig. 2K), consistent with topological defects in 2D phase oscillator systems that can transiently stabilize (*81*, *82*). In the desynchronized regime, there were many defects (including rotating waves) with very short lifetimes as they bounced around and annihilated each other under noisy driving. In the synchronized regime, the dominant defect was the rotating waves because they were topologically protected against continuous deformations leaving them only to find an opposite rotating wave to annihilate or leave/enter through the boundary of the domain (*81*, *82*).

Comparison of isotropic model and circular bias model: To compare the isotropic model and circular bias model, we first simulated 100 random seeds with the same initial condition, coupling strength scale $K = 1$ and noise scale $I = 0$. We observed that the rotation indices in the final frame of the simulation were significantly higher in the circular bias model, compared with the isotropic model (fig. S10, D and E). In a set of 25 random seeds, we compared the rotation index as a function of coupling strength scale K and noise scale $I(t)$ (Fig. 2K). We used the same initial conditions for all comparisons. Coupling strength of the network increased linearly by dialing up the coupling strength scale K between 0 and 4 along the x axis of the phase space sweep (Fig. 2K). The temporally correlated noise term $I(t)$ was sampled from Gaussian distribution ~N(0, noise_scale), with its magnitude tuned by the standard deviation of the normal distribution between 0 and 30 in the y axis of the phase space sweep (Fig. 2K).

Mirror symmetry model: To explore how mirror symmetry (Fig. 3) affects the rotating wave distribution, we constructed a mirror symmetry model (fig. S10, F to J). We filled 4000 cells in the bottom right quadrant of the 2d space first with random normal distribution, with effective coupling weight between each cell pair defined as an exponential decay function proportional to the Euclidean distance between them (similar to the isotropic model above). We then flipped a random quarter of cells to one of the remaining three quadrants of the 2D space (repeated 3×), and kept the cell-pair weights defined before flip. By doing so, we created a mirror symmetry model, where the cell positions and connectivity weights were mirrored in neighboring quadrants (cell pairs that were close in space before flip were still tightly coupled after flip, despite flipped quadrant position), and local connectivity within a single quadrant was still preserved. To construct a nonsymmetrical model in comparison to the mirror symmetry model (fig. S10F), we kept the cell positions after the flip in the mirror symmetry model, but re-calculated the cell-pair weights with exponential decaying function across all cells (no quadrant symmetry). Weight matrix was normalized by the mean weights of all cell pairs in both isotropic model and mirror symmetry model, for a fair comparison. We simulated 450 random seeds with the same initial condition for both models. Rotating wave centers were detected in each simulation seed with a rotating wave detection algorithm as in wide-field imaging data, and concatenated across 450 seeds for comparison. Rotating wave density was normalized to the same peak density value for model comparison. An absence of rotating wave centers along the borders in the mirror symmetry model was observed, as in the wide-field imaging data.

Linear regression within cortex (Fig. 3 and fig. S11)

Reduced rank regression was applied to predict the posterior sensory cortical activity from the anterior motor cortex, and to predict the right hemisphere from the left hemisphere. Reduced rank regression has the advantage of finding the subspace of regressor activity that is maximally predictive of the target activity, thus acting as both a regularization and a characterization of dimensionality (*128*). To divide the anterior/posterior cortex as regressor and target, wide-field data (X*Y*t) was first registered to Allen CCF coordinates (*85*), and divided into anterior cortical data and posterior cortical data along the border of SSp and MOp respecting the connectivity reciprocity (*41*) and rotating wave symmetry we observed. To divide the left/right cortex, the midline was chosen as the dividing line after registration. The first 20 min of the wide-field data in each session was used as training data, and a 10-min data section after the training data was used as testing data for cross validation. To account for data collinearity, we applied singular value decomposition ($D = USV^T$) on the regressor data and used the top 50 temporal components (S*V) as the regressor in the regression model, which accounted for 97.3 ± 0.5% (mean ± SEM, 15 mice) of total variance before compression, as previously stated in the Materials and methods section "Wide-field imaging and data processing" section. The target data were kept in the original data space (pixels*t). Prediction accuracy was calculated using the coefficient of determination (R^2) on the testing dataset:

$$R^2 = 1 - \frac{SS_{\text{res}}}{SS_{\text{tot}}}, \text{where } SS_{\text{res}} = \sum_i (y_i - \hat{y}_i)^2, SS_{\text{tot}} = \sum_i (y_i - \bar{y})^2$$

Where SS_{res} is the residual sum of squares, SS_{tot} is the total sum of squares, y_i is the i-th value in the observed data, $\hat{y}_i$ is the predicted data, and $\bar{y}$ is the mean of the observed data.

To visualize the regression kernel representation in the cortex space, the regression kernel was first transformed back to the pixel space. Kernel maps for example pixels were presented as different color plots overlaid with transparency scaled by kernel weights (Fig. 3, E to J, and fig. S11). Example regressor pixels in Fig. 3, E and F were chosen as the pixel with maximum value in the weight matrix.

To investigate the matching probability of rotating waves between observed activity and predicted activity from the contralateral hemisphere, we constructed a linear regression model to predict wide-field activity across the cortex using activity from the right sensory cortex (or motor cortex). We then compared the directions of observed and predicted rotating waves in the left hemisphere (or sensory cortex). The full duration of the data was predicted with two-fold cross-validation. In detail, we split the data into 10 equal-length epochs, with the five odd-numbered epochs concatenated to predict the held-out

even epochs, and vice versa. Shuffle data were constructed by randomly permuting the identities of the 50 temporal components in the held-out data, without retraining the regression model.

Bulk axon projection map and matching index (Fig. 3)

To visualize the long range axon projection maps from sensory cortex to the contralateral hemisphere, or to the motor cortex, we selected eight viral tracer injection experiments targeting eight different sensory modalities within the sensory cortex from the Allen Mouse Brain Connectivity Atlas (*46*). The same session IDs were used to identify Neuropixels targeting angles and positions in the subcortical areas in Materials and methods section "Simultaneous Neuropixels recording and wide-field imaging." To combine axon projection maps together, intensity values for injection sites in the sensory cortex were masked first and then normalized across sessions to account for intensity differences between injection site and target axon region, as well as differences across sessions respectively.

To quantify whether the activity kernel patterns and axon projection patterns matched, we designed a pattern matching index (P_{index}) which is the sum of matrix dot product between activity kernel and axon projection map of the same size across all eight different sampled sensory areas:

$$P_{\text{index}} = \sum_{i=1}^{n} \text{dot}(A_i, B_i)$$

where A_i is the activity kernel for one of the n ($n = 8$) sampled sensory areas, B_i is the axon projection map for one of the eight sampled sensory areas.

We used a single common axon projection session for each of eight sensory areas to compute the matching index, together with mean activity maps across 15 mice. Small variations were observed between the activity map and the axon projection map due to variations of brain registration for each mouse, as well as the slight difference of sampling points for activity map and projection maps. However, the general patterns of both maps matched well for left-to-right hemispheres (Fig. 3, G and H) and motor-to-sensory cortex (Fig. 3, I and J), compared with permutation. Permutation was performed by randomizing the identity of the 8 axon projection maps 1000 times. For visualization purposes, we normalized pattern matching index in real data and permutation by the minimum and maximum values in the permutation set and real data together, ensuring all values are within [0,1] index scale.

Bilateral cutting experiment within the somatosensory cortex (Fig. 3)

At least one session of spontaneous wide-field activity was recorded to identify rotating wave centers before incision experiments. The centers of the craniotomy and incision were positioned near the peak rotating wave density point (<1 to 1.5 mm) in the middle of somatosensory cortex. Mice were anaesthetized for craniotomy and incision procedures as described in the Materials and methods section "Surgery." Craniotomies were ~1 mm in diameter. Bilateral cortical cuts were performed with a micro surgical knife (Fine Science Tools, catalog no. 10318-14) using a single cut to a depth of 1.5 mm from the cortical surface, with an incision width of less than 0.5 mm. The microsurgical knife was mounted on a manipulator arm of a stereotaxic instrument and was held at the target depth for at least 2 min before retraction. Craniotomies and incisions were then covered with dural gel, and a protective plastic cap was attached to the recording chamber before the mouse recovered from surgery.

Rotating wave prediction from subcortical spiking activity (Fig. 4 and fig. S12)

Kilosort2 (*109*) was used for spike sorting of the electrophysiology data from four-shank Neuropixels recordings. Single neurons were manually curated through Phy (https://github.com/cortex-lab/phy), with violation of refractory period in spike time auto-correlogram as the main criteria for selection. Spikes of each single neuron were then binned at the wide-field imaging sampling frequency (35 Hz) to match the time series of the imaging data.

To predict cortical wide-field data from subcortical spike data (Fig. 4, B and C), time series of spiking neurons were used to predict the derivative of top 50 temporal components of the cortical wide-field data. To predict the full length of the wide-field data from subcortical spiking activity, we used 2-fold cross-validation. In detail, we first split the data into 10 equal-length epochs. Then we used the concatenated five odd-numbered epochs to predict the held-out even epochs, and vice versa. The mean variance explained map was calculated as the average of the two predictions. To account for the latency between cortical wide-field data and spike data, time-shifted spiking series from –17 to 17 samples (–0.5 to 0.5 s at ~0.03-s time steps) were also concatenated into the regressor matrix. For quality control purposes, only sessions with mean variance explained exceeding 10% were included for further analysis (32/46 sessions).

To compare rotating waves in the raw and predicted cortical activity (Fig. 4G), we took the derivative of the temporal components of the raw and predicted data, and reconstructed the data in pixel space ($X*Y*t$) after a bandpass 2- to 8-Hz filter. We then detected rotating waves in both raw and predicted cortical data by applying the automated rotating wave detection algorithm. Rotating waves in the raw cortical activity with significant radius (greater than or equal to 0.69 mm) and duration (>29 ms), were considered for rotating wave direction comparison. Selection criteria were not applied to the predicted rotating waves, to maximize the numbers of corresponding rotating waves included in the subsequent matching test. For each rotating wave in the raw cortical activity, if only one corresponding rotating wave was found within 1 mm radius in the predicted cortical activity in the same frame, then the pair of rotating waves was considered as a candidate pair. We then compared the rotating wave directions (clockwise or counterclockwise) for all pairs of candidate rotating waves, and computed the rotating wave matching probability as the ratio of matching rotating wave pairs out of all candidate rotating wave pairs. Here, "matching" means that the raw and predicted rotating waves share the same direction. To test the null hypothesis that neurons in the subcortical area did not share spatiotemporal relationships with the cortical data, and that matching rotating waves therefore only arose by chance, we computed the matching probability with permuted spiking data. We first predicted cortical activity by using subcortical spiking activity with permuted neuron identities during linear regression prediction without retraining the model, and then applied the same automated rotating wave detection algorithm for the permuted prediction. We then computed the rotating wave matching probability between the raw and permuted prediction as control.

Traveling wave quantification with optical flow (Fig. 4 and figs. S12 and S13)

To quantify traveling waves within the cortical wide-field activity (Fig. 4 and fig. S12), we estimated instantaneous velocity for each pixel in the cortex using phase information from nearby two frames. In detail, the derivative of the wide-field data was first bandpass Butterworth filtered within 2 to 8 Hz, and the Hilbert transform was then applied to each pixel independently to extract phase information at each time point to construct the phase maps. We then applied the Horn-Schunck method (*126*) to extract optical flow from the phase maps of adjacent frames, which used an optimization approach to estimate instantaneous velocity with a global constraint of smoothness.

To compare phase maps and traveling waves of the raw and predicted cortical activity from subcortical spiking activity (Fig. 4, H and I, and fig. S13F), we designed frame-to-frame "phase matching index" and "traveling wave matching index." First, the angular differences of the phase values or the optical flow vectors between raw and predicted

data were calculated for pixels in each frame with frame size [m,n]. Phase or traveling wave matching index (M) is the mean resultant vector length of the angular difference map in a frame:

$$M = \frac{\left|\sum_{x=1}^{m}\sum_{y=1}^{n} e^{i\cdot\theta_{x,y}}\right|}{m \times n}$$

where $\theta_{x,y}$ is the phase angular differences of the [x, y]-th pixel between a raw and predicted frame. M index is bound between 0 and 1. M close to 0 indicates all angular difference values are randomly distributed and not matching, and M close to 1 indicates all angular difference values are uniformly distributed and matching.

To summarize the observation that phase or traveling wave matching index increased as mean 2- to 8-Hz amplitude in the cortex increased within a session (Fig. 4, H and I, and fig. S13F), we binned frames based on the mean 2- to 8-Hz amplitude and calculated the mean matching index within each amplitude bin. Only pixels with cross-validated variance explained >0.1 were included in the final phase or wave matching index calculation. To construct the null distribution, we used the same strategy as described above for rotating wave matching, by randomizing the subcortical neuron identities in the testing dataset for regression prediction 20 times, without retraining the model. Phase and wave matching index were then calculated between the raw phase (or traveling waves) and permuted predictions, as control distributions.

Passive air puff experiment on the whisker pad (Fig. 5)

Air puffs were delivered from compressed air to a blunt-tip dispensing needle (inner diameter: 1mm) through a thin connecting tubing (inner diameter: 0.78 mm). The needle tip was mounted on a manipulator and positioned close to the whisker pad (<0.5 to 1 cm), ensuring the air puff affected only the local facial area. Each session consisted of 1000 air puffs, with each puff lasting 30 ms. Intertrial intervals were drawn randomly from an exponential decay distribution ranging from 1 to 6 s, with a mean of 3 s. Each session lasted 50 to 60 min.

Two-alternative choice task (Fig. 6 and figs. S14 and S15)

The two-alternative choice task was closely based on the visual detection tasks described in prior work (*83*, *84*). We trained four jGCaMP8s transgenic mice, with details in the Materials and methods section "Animals and virus injections."

Mice underwent training in two stages. The first stage focused on the primary task structure using only 100% contrast stimuli, which took 2 to 10 weeks. During this stage, mice held the wheel stationary for 200 to 500 ms before a Gabor patch stimulus appeared on either the left or right side of the screen. A 5-kHz tone indicated the start of the trial. Mice moved the stimulus to the center of the screen, by turning the wheel at least ~20 mm in the correct direction, with movement coupled to the stimulus in a closed-loop setup. From the mouse's perspective, they need to move the wheel clockwise for a stimulus on the left screen, and counterclockwise for a stimulus on the right screen. Correct responses were rewarded with 2 to 3 μl of 10% sucrose water dispensed through a trigger-controlled valve on the water tube, whereas incorrect response or inactivity within 30 s resulted in a white noise beep of 0.5 s indicating failure or time-out. Trials were separated by an average intertrial interval (ITI) of 500 ms. Mice received at least 1.5 ml of water by the end of the day regardless of task performance. Once mice achieved >80% accuracy, they were moved to the next training stage.

In the second stage, auditory cues were removed, requiring reliance solely on the visual stimulus. Lower-contrast stimuli (50%, 25%, 12%, and 6%) were gradually introduced. Mice had to hold the wheel still for at least 0.4 s (exponential decay distribution, with a mean of 0.7 s, range between 0.4 and 3 s) before stimulus onset, with a response window reduced to 2 to 5 s before a trial time-out. Training was complete when mice reached at least 80% accuracy for combined 50% and 100% contrast trials combined for both sides, regardless of performance at lower contrast levels.

After completing task training, mice were transferred to the wide-field imaging station for data collection. To ensure consistent performance on both sides, trials with 50% and 100% contrast stimuli were repeated until mice made correct choices, whereas trials with contrasts below 50% were only presented once per initiated trial. High-contrast trials were included at a higher ratio to maintain motivation to perform the task. The average trial ratio for each session was approximately [1:0.8:0.5:0.5:0.5:0.2] for contrasts at [100%:50%:25%:12%:6%:0%], respectively.

A total of four mice successfully learned the task, completing 3866 ± 1165 trials (mean ± SEM) for 5 to 11 sessions (fig. S15A). At the end of each experimental day, wide-field imaging data were also collected under passive viewing conditions, where the reward port was withdrawn. For each passive viewing session, 100 passive trials were presented at each of 11 different contrast levels, randomly displayed on either the left or right side of the screen. The inter-trial interval ranged from 0.5 to 3 s, with a mean duration of 1 s.

Within-subject permutation test (Fig. 6)

To account for the rich session numbers (repeated measures design) but limited total subjects (n = 4 mice) of our visuomotor behavior dataset, we used a within-subject permutation test to compare paired time points for increased statistical power without normality assumptions. We calculated the observed effect as the mean difference between two time points, then generated a null distribution through 10,000 permutations where time point labels were randomly assigned within each subject independently. This preserves within-subject correlations while testing for systematic time effects. The two-tailed P value represented the proportion of permuted effects exceeding the observed effect.

REFERENCES AND NOTES

1. G. B. Ermentrout, D. Kleinfeld, Traveling electrical waves in cortex: Insights from phase dynamics and speculation on a computational role. *Neuron* **29**, 33–44 (2001). doi: 10.1016/S0896-6273(01)00178-7; pmid: 11182079
2. L. Muller, F. Chavane, J. Reynolds, T. J. Sejnowski, Cortical travelling waves: Mechanisms and computational principles. *Nat. Rev. Neurosci.* **19**, 255–268 (2018). doi: 10.1038/nrn.2018.20; pmid: 29563572
3. J.-Y. Wu, Xiaoying Huang, Chuan Zhang, Propagating waves of activity in the neocortex: What they are, what they do. *Neuroscientist* **14**, 487–502 (2008). doi: 10.1177/1073858408317066; pmid: 18997124
4. W. J. Freeman, Waves, pulses, and the theory of neural masses. *Prog. Theor. Biol.* **2**, 87–165 (1972). doi: 10.1016/B978-0-12-543102-6.50010-8
5. J. C. Prechtl, L. B. Cohen, B. Pesaran, P. P. Mitra, D. Kleinfeld, Visual stimuli induce waves of electrical activity in turtle cortex. *Proc. Natl. Acad. Sci. U.S.A.* **94**, 7621–7626 (1997). doi: 10.1073/pnas.94.14.7621; pmid: 9207142
6. M. P. Vanni, A. W. Chan, M. Balbi, G. Silasi, T. H. Murphy, Mesoscale mapping of mouse cortex reveals frequency-dependent cycling between distinct macroscale functional modules. *J. Neurosci.* **37**, 7513–7533 (2017). doi: 10.1523/JNEUROSCI.3560-16.2017; pmid: 28674167
7. R. G. Townsend, P. Gong, Detection and analysis of spatiotemporal patterns in brain activity. *PLOS Comput. Biol.* **14**, e1006643 (2018). doi: 10.1371/journal.pcbi.1006643; pmid: 30507937
8. M. H. Mohajerani, D. A. McVea, M. Fingas, T. H. Murphy, Mirrored bilateral slow-wave cortical activity within local circuits revealed by fast bihemispheric voltage-sensitive dye imaging in anesthetized and awake mice. *J. Neurosci.* **30**, 3745–3751 (2010). doi: 10.1523/JNEUROSCI.6437-09.2010; pmid: 20220008
9. R. A. Swanson *et al.*, Topography of putative bi-directional interaction between hippocampal sharp-wave ripples and neocortical slow oscillations. *Neuron* **113**, 754–768.e9 (2025). doi: 10.1016/j.neuron.2024.12.019; pmid: 39874961
10. X. Huang *et al.*, Spiral wave dynamics in neocortex. *Neuron* **68**, 978–990 (2010). doi: 10.1016/j.neuron.2010.11.007; pmid: 21145009
11. J. Viventi *et al.*, Flexible, foldable, actively multiplexed, high-density electrode array for mapping brain activity in vivo. *Nat. Neurosci.* **14**, 1599–1605 (2011). doi: 10.1038/nn.2973; pmid: 22081157

12. S. Bhattacharya, S. L. Brincat, M. Lundqvist, E. K. Miller, Traveling waves in the prefrontal cortex during working memory. *PLOS Comput. Biol.* **18**, e1009827 (2022). doi: 10.1371/journal.pcbi.1009827; pmid: 35089915
13. M. Denker *et al.*, LFP beta amplitude is linked to mesoscopic spatio-temporal phase patterns. *Sci. Rep.* **8**, 5200 (2018). doi: 10.1038/s41598-018-22990-7; pmid: 29581430
14. E. Torre *et al.*, Synchronous spike patterns in macaque motor cortex during an instructed-delay reach-to-grasp task. *J. Neurosci.* **36**, 8329–8340 (2016). doi: 10.1523/JNEUROSCI.4375-15.2016; pmid: 27511007
15. L. Muller *et al.*, Rotating waves during human sleep spindles organize global patterns of activity that repeat precisely through the night. *eLife* **5**, e17267 (2016). doi: 10.7554/eLife.17267; pmid: 27855061
16. R. V. Raut *et al.*, Global waves synchronize the brain's functional systems with fluctuating arousal. *Sci. Adv.* **7**, eabf2709 (2021). doi: 10.1126/sciadv.abf2709; pmid: 34290088
17. Y. Xu, X. Long, J. Feng, P. Gong, Interacting spiral wave patterns underlie complex brain dynamics and are related to cognitive processing. *Nat. Hum. Behav.* **7**, 1196–1215 (2023). doi: 10.1038/s41562-023-01626-5; pmid: 37322235
18. A. Alamia, R. VanRullen, Alpha oscillations and traveling waves: Signatures of predictive coding? *PLOS Biol.* **17**, e3000487 (2019). doi: 10.1371/journal.pbio.3000487; pmid: 31581198
19. D. M. Alexander, L. Dugué, The dominance of global phase dynamics in human cortex, from delta to gamma. *eLife* **13**, RP100674 (2024). doi: 10.7554/eLife.100674; pmid: 41954599
20. D. P. Koller, M. Schirner, P. Ritter, Human connectome topology directs cortical traveling waves and shapes frequency gradients. *Nat. Commun.* **15**, 3570 (2024). doi: 10.1038/s41467-024-47860-x; pmid: 38670965
21. Y. Xu *et al.*, Spatiotemporal dynamics of sleep spindles form spiral waves that predict overnight memory consolidation and age-related memory decline. *Commun. Biol.* **8**, 1014 (2025). doi: 10.1038/s42003-025-08447-4; pmid: 40624137
22. Z. W. Davis, L. Muller, J. Martinez-Trujillo, T. Sejnowski, J. H. Reynolds, Spontaneous travelling cortical waves gate perception in behaving primates. *Nature* **587**, 432–436 (2020). doi: 10.1038/s41586-020-2802-y; pmid: 33029013
23. R. F. Helfrich *et al.*, Neural mechanisms of sustained attention are rhythmic. *Neuron* **99**, 854–865.e5 (2018). doi: 10.1016/j.neuron.2018.07.032; pmid: 30138591
24. T. K. Sato, I. Nauhaus, M. Carandini, Traveling waves in visual cortex. *Neuron* **75**, 218–229 (2012). doi: 10.1016/j.neuron.2012.06.029; pmid: 22841308
25. W. J. Freeman, Spatial properties of an EEG event in the olfactory bulb and cortex. *Electroencephalogr. Clin. Neurophysiol.* **44**, 586–605 (1978). doi: 10.1016/0013-4694(78)90126-8; pmid: 77765
26. E. V. Lubenov, A. G. Siapas, Hippocampal theta oscillations are travelling waves. *Nature* **459**, 534–539 (2009). doi: 10.1038/nature08010; pmid: 19489117
27. J. Patel, S. Fujisawa, A. Berényi, S. Royer, G. Buzsáki, Traveling theta waves along the entire septotemporal axis of the hippocampus. *Neuron* **75**, 410–417 (2012). doi: 10.1016/j.neuron.2012.07.015; pmid: 22884325
28. H. Zhang, J. Jacobs, Traveling theta waves in the human hippocampus. *J. Neurosci.* **35**, 12477–12487 (2015). doi: 10.1523/JNEUROSCI.5102-14.2015; pmid: 26354915
29. D. Rubino, K. A. Robbins, N. G. Hatsopoulos, Propagating waves mediate information transfer in the motor cortex. *Nat. Neurosci.* **9**, 1549–1557 (2006). doi: 10.1038/nn1802; pmid: 17115042
30. K. Takahashi *et al.*, Large-scale spatiotemporal spike patterning consistent with wave propagation in motor cortex. *Nat. Commun.* **6**, 7169 (2015). doi: 10.1038/ncomms8169; pmid: 25994554
31. L. Muller, A. Reynaud, F. Chavane, A. Destexhe, The stimulus-evoked population response in visual cortex of awake monkey is a propagating wave. *Nat. Commun.* **5**, 3675 (2014). doi: 10.1038/ncomms4675; pmid: 24770473
32. T. P. Zanos, P. J. Mineault, K. T. Nasiotis, D. Guitton, C. C. Pack, A sensorimotor role for traveling waves in primate visual cortex. *Neuron* **85**, 615–627 (2015). doi: 10.1016/j.neuron.2014.12.043; pmid: 25600124
33. S. Chemla *et al.*, Suppressive traveling waves shape representations of illusory motion in primary visual cortex of awake primate. *J. Neurosci.* **39**, 4282–4298 (2019). doi: 10.1523/JNEUROSCI.2792-18.2019; pmid: 30886010
34. A. Alamia, R. VanRullen, A traveling waves perspective on temporal binding. *J. Cogn. Neurosci.* **36**, 721–729 (2024). doi: 10.1162/jocn_a_02004; pmid: 37172133
35. M. M. Mesulam, From sensation to cognition. *Brain* **121**, 1013–1052 (1998). doi: 10.1093/brain/121.6.1013; pmid: 9648540
36. M. N. Oude Lohuis, P. Marchesi, U. Olcese, C. M. A. Pennartz, Triple dissociation of visual, auditory and motor processing in mouse primary visual cortex. *Nat. Neurosci.* **27**, 758–771 (2024). doi: 10.1038/s41593-023-01564-5; pmid: 38307971
37. A. R. Garner, G. B. Keller, A cortical circuit for audio-visual predictions. *Nat. Neurosci.* **25**, 98–105 (2022). doi: 10.1038/s41593-021-00974-7; pmid: 34857950
38. C. Cappe, P. Barone, Heteromodal connections supporting multisensory integration at low levels of cortical processing in the monkey. *Eur. J. Neurosci.* **22**, 2886–2902 (2005). doi: 10.1111/j.1460-9568.2005.04462.x; pmid: 16324124
39. A. A. Ghazanfar, C. E. Schroeder, Is neocortex essentially multisensory? *Trends Cogn. Sci.* **10**, 278–285 (2006). doi: 10.1016/j.tics.2006.04.008; pmid: 16713325
40. W. Penfield, E. Boldrey, Somatic motor and sensory representation in the cerebral cortex of man as studied by electrical stimulation. *Brain* **60**, 389–443 (1937). doi: 10.1093/brain/60.4.389
41. B. Zingg *et al.*, Neural networks of the mouse neocortex. *Cell* **156**, 1096–1111 (2014). doi: 10.1016/j.cell.2014.02.023; pmid: 24581503
42. J. H. Kaas, Topographic maps are fundamental to sensory processing. *Brain Res. Bull.* **44**, 107–112 (1997). doi: 10.1016/S0361-9230(97)00094-4; pmid: 9292198
43. A. A. Hamid, M. J. Frank, C. I. Moore, Wave-like dopamine dynamics as a mechanism for spatiotemporal credit assignment. *Cell* **184**, 2733–2749.e16 (2021). doi: 10.1016/j.cell.2021.03.046; pmid: 33861952
44. N. L. Benavidez *et al.*, Organization of the inputs and outputs of the mouse superior colliculus. *Nat. Commun.* **12**, 4004 (2021). doi: 10.1038/s41467-021-24241-2; pmid: 34183678
45. H. Hintiryan *et al.*, The mouse cortico-striatal projectome. *Nat. Neurosci.* **19**, 1100–1114 (2016). doi: 10.1038/nn.4332; pmid: 27322419
46. S. W. Oh *et al.*, A mesoscale connectome of the mouse brain. *Nature* **508**, 207–214 (2014). doi: 10.1038/nature13186; pmid: 24695228
47. M. H. Mohajerani *et al.*, Spontaneous cortical activity alternates between motifs defined by regional axonal projections. *Nat. Neurosci.* **16**, 1426–1435 (2013). doi: 10.1038/nn.3499; pmid: 23974708
48. A. J. Peters, J. M. J. Fabre, N. A. Steinmetz, K. D. Harris, M. Carandini, Striatal activity topographically reflects cortical activity. *Nature* **591**, 420–425 (2021). doi: 10.1038/s41586-020-03166-8; pmid: 33473213
49. D. Shimaoka, N. A. Steinmetz, K. D. Harris, M. Carandini, The impact of bilateral ongoing activity on evoked responses in mouse cortex. *eLife* **8**, e43533 (2019). doi: 10.7554/eLife.43533; pmid: 31038456
50. S. Grün *et al.*, Emerging principles of spacetime in brains: Meeting report on spatial neurodynamics. *Neuron* **110**, 1894–1898 (2022). doi: 10.1016/j.neuron.2022.05.018; pmid: 35709696
51. J. C. Pang *et al.*, Geometric constraints on human brain function. *Nature* **618**, 566–574 (2023). doi: 10.1038/s41586-023-06098-1; pmid: 37258669
52. L. F. Rossi, R. C. Wykes, D. M. Kullmann, M. Carandini, Focal cortical seizures start as standing waves and propagate respecting homotopic connectivity. *Nat. Commun.* **8**, 217 (2017). doi: 10.1038/s41467-017-00159-6; pmid: 28794407
53. J. B. Ackman, T. J. Burbridge, M. C. Crair, Retinal waves coordinate patterned activity throughout the developing visual system. *Nature* **490**, 219–225 (2012). doi: 10.1038/nature11529; pmid: 23060192
54. V. Moreno-Juan *et al.*, Prenatal thalamic waves regulate cortical area size prior to sensory processing. *Nat. Commun.* **8**, 14172 (2017). doi: 10.1038/ncomms14172; pmid: 28155854
55. M. T. Kaufman, M. M. Churchland, S. I. Ryu, K. V. Shenoy, Cortical activity in the null space: Permitting preparation without movement. *Nat. Neurosci.* **17**, 440–448 (2014). doi: 10.1038/nn.3643; pmid: 24487233
56. J. D. Semedo, A. Zandvakili, C. K. Machens, B. M. Yu, A. Kohn, Cortical areas interact through a communication subspace. *Neuron* **102**, 249–259.e4 (2019). doi: 10.1016/j.neuron.2019.01.026; pmid: 30770252
57. D. B. Nestvogel, D. A. McCormick, Visual thalamocortical mechanisms of waking state-dependent activity and alpha oscillations. *Neuron* **110**, 120–138.e4 (2022). doi: 10.1016/j.neuron.2021.10.005; pmid: 34687663
58. Y. Senzai, A. Fernandez-Ruiz, G. Buzsáki, Layer-specific physiological features and interlaminar interactions in the primary visual cortex of the mouse. *Neuron* **101**, 500–513.e5 (2019). doi: 10.1016/j.neuron.2018.12.009; pmid: 30635232
59. C. Bennett *et al.*, SHIELD: Skull-shaped hemispheric implants enabling large-scale electrophysiology datasets in the mouse brain. *Neuron* **112**, 2869–2885.e8 (2024). doi: 10.1016/j.neuron.2024.06.015; pmid: 38996587
60. M. C. Einstein, P.-O. Polack, D. T. Tran, P. Golshani, Visually evoked 3–5 Hz membrane potential oscillations reduce the responsiveness of visual cortex neurons in awake behaving mice. *J. Neurosci.* **37**, 5084–5098 (2017). doi: 10.1523/JNEUROSCI.3868-16.2017; pmid: 28432140
61. E. A. K. Jacobs, N. A. Steinmetz, A. J. Peters, M. Carandini, K. D. Harris, Cortical State Fluctuations during Sensory Decision Making. *Curr. Biol.* **30**, 4944–4955.e7 (2020). doi: 10.1016/j.cub.2020.09.067; pmid: 33096037
62. G. Buzsáki, *Rhythms of the Brain* (Oxford Univ. Press, 2006), .doi: 10.1093/acprof:oso/9780195301069.001.0001
63. K. L. Anderson, M. Ding, Attentional modulation of the somatosensory mu rhythm. *Neuroscience* **180**, 165–180 (2011). doi: 10.1016/j.neuroscience.2011.02.004; pmid: 21310216
64. Y. Orsher *et al.*, Sequentially activated discrete modules appear as traveling waves in neuronal measurements with limited spatiotemporal sampling. *eLife* **12**, RP92254 (2024). doi: 10.7554/eLife.92254; pmid: 38451063
65. D. Prichard, J. Theiler, Generating surrogate data for time series with several simultaneously measured variables. *Phys. Rev. Lett.* **73**, 951–954 (1994). doi: 10.1103/PhysRevLett.73.951; pmid: 10057582
66. A. Das, E. Zabeh, B. Ermentrout, J. Jacobs, Planar, spiral, and concentric traveling waves distinguish cognitive states in human memory. bioRxiv 577456 [Preprint] (2024); https://doi.org/10.1101/2024.01.26.577456.

67. S. Grødem *et al.*, An updated suite of viral vectors for in vivo calcium imaging using intracerebral and retro-orbital injections in male mice. *Nat. Commun.* **14**, 608 (2023). doi: 10.1038/s41467-023-36324-3; pmid: 36739289
68. H. Dana *et al.*, High-performance calcium sensors for imaging activity in neuronal populations and microcompartments. *Nat. Methods* **16**, 649–657 (2019). doi: 10.1038/s41592-019-0435-6; pmid: 31209382
69. Y. Zhang *et al.*, Fast and sensitive GCaMP calcium indicators for imaging neural populations. *Nature* **615**, 884–891 (2023). doi: 10.1038/s41586-023-05828-9; pmid: 36922596
70. A. E. Telfeian, B. W. Connors, Widely integrative properties of layer 5 pyramidal cells support a role for processing of extralaminar synaptic inputs in rat neocortex. *Neurosci. Lett.* **343**, 121–124 (2003). doi: 10.1016/S0304-3940(03)00379-3; pmid: 12759179
71. H. A. Swadlow, Efferent neurons and suspected interneurons in S-1 vibrissa cortex of the awake rabbit: Receptive fields and axonal properties. *J. Neurophysiol.* **62**, 288–308 (1989). doi: 10.1152/jn.1989.62.1.288; pmid: 2754479
72. H. Peng *et al.*, Morphological diversity of single neurons in molecularly defined cell types. *Nature* **598**, 174–181 (2021). doi: 10.1038/s41586-021-03941-1; pmid: 34616072
73. T. E. Lee, H. Tam, G. Refael, J. L. Rogers, M. C. Cross, Vortices and the entrainment transition in the two-dimensional Kuramoto model. *Phys. Rev. E Stat. Nonlin. Soft Matter Phys.* **82**, 036202 (2010). doi: 10.1103/PhysRevE.82.036202; pmid: 21230156
74. B. Ottino-Löffler, S. H. Strogatz, Frequency spirals. *Chaos* **26**, 094804 (2016). doi: 10.1063/1.4954038; pmid: 27781469
75. B. Ermentrout, Y. Park, D. Wilson, Recent advances in coupled oscillator theory. *Philos. Trans. A Math. Phys. Eng. Sci.* **377**, 20190092 (2019). pmid: 31656142
76. G. B. Ermentrout, Stable periodic solutions to discrete and continuum arrays of weakly coupled nonlinear oscillators. *SIAM J. Appl. Math.* **52**, 1665–1687 (1992). doi: 10.1137/0152096
77. J. E. Paullet, G. B. Ermentrout, Stable rotating waves in two-dimensional discrete active media. *SIAM J. Appl. Math.* **54**, 1720–1744 (1994). doi: 10.1137/S0036139993250683
78. Z. W. Davis *et al.*, Spontaneous traveling waves naturally emerge from horizontal fiber time delays and travel through locally asynchronous-irregular states. *Nat. Commun.* **12**, 6057 (2021). doi: 10.1038/s41467-021-26175-1; pmid: 34663796
79. G. B. Benigno, R. C. Budzinski, Z. W. Davis, J. H. Reynolds, L. Muller, Waves traveling over a map of visual space can ignite short-term predictions of sensory input. *Nat. Commun.* **14**, 3409 (2023). doi: 10.1038/s41467-023-39076-2; pmid: 37296131
80. B. Hellwig, A quantitative analysis of the local connectivity between pyramidal neurons in layers 2/3 of the rat visual cortex. *Biol. Cybern.* **82**, 111–121 (2000). doi: 10.1007/PL00007964; pmid: 10664098
81. V. Flovik, F. Macià, E. Wahlström, Describing synchronization and topological excitations in arrays of magnetic spin torque oscillators through the Kuramoto model. *Sci. Rep.* **6**, 32528 (2016). doi: 10.1038/srep32528; pmid: 27580938
82. M. Sarkar, N. Gupte, Phase synchronization in the two-dimensional Kuramoto model: Vortices and duality. *Phys. Rev. E* **103**, 032204 (2021). doi: 10.1103/PhysRevE.103.032204; pmid: 33862679
83. C. P. Burgess *et al.*, High-yield methods for accurate two-alternative visual psychophysics in head-fixed mice. *Cell Rep.* **20**, 2513–2524 (2017). doi: 10.1016/j.celrep.2017.08.047; pmid: 28877482
84. N. A. Steinmetz, P. Zatka-Haas, M. Carandini, K. D. Harris, Distributed coding of choice, action and engagement across the mouse brain. *Nature* **576**, 266–273 (2019). doi: 10.1038/s41586-019-1787-x; pmid: 31776518
85. Q. Wang *et al.*, The Allen Mouse Brain Common Coordinate Framework: A 3D Reference Atlas. *Cell* **181**, 936–953.e20 (2020). doi: 10.1016/j.cell.2020.04.007; pmid: 32386544
86. H. Osaki, M. Kanaya, Y. Ueta, M. Miyata, Distinct nociception processing in the dysgranular and barrel regions of the mouse somatosensory cortex. *Nat. Commun.* **13**, 3622 (2022). doi: 10.1038/s41467-022-31272-w; pmid: 35768422
87. T. Lee, U. Kim, Descending projections from the dysgranular zone of rat primary somatosensory cortex processing deep somatic input. *J. Comp. Neurol.* **520**, 1021–1046 (2012). doi: 10.1002/cne.22767; pmid: 21935942
88. C. C. H. Petersen, A. Grinvald, B. Sakmann, Spatiotemporal dynamics of sensory responses in layer 2/3 of rat barrel cortex measured in vivo by voltage-sensitive dye imaging combined with whole-cell voltage recordings and neuron reconstructions. *J. Neurosci.* **23**, 1298–1309 (2003). doi: 10.1523/JNEUROSCI.23-04-01298.2003; pmid: 12598618
89. C. C. H. Petersen, T. T. G. Hahn, M. Mehta, A. Grinvald, B. Sakmann, Interaction of sensory responses with spontaneous depolarization in layer 2/3 barrel cortex. *Proc. Natl. Acad. Sci. U.S.A.* **100**, 13638–13643 (2003). doi: 10.1073/pnas.2235811100; pmid: 14595013
90. R. T. Narayanan *et al.*, Beyond columnar organization: Cell type- and target layer-specific principles of horizontal axon projection patterns in rat vibrissal cortex. *Cereb. Cortex* **25**, 4450–4468 (2015). doi: 10.1093/cercor/bhv053; pmid: 25838038
91. R. O. L. Wong, Retinal waves and visual system development. *Annu. Rev. Neurosci.* **22**, 29–47 (1999). doi: 10.1146/annurev.neuro.22.1.29; pmid: 10202531
92. R. Khazipov *et al.*, Early motor activity drives spindle bursts in the developing somatosensory cortex. *Nature* **432**, 758–761 (2004). doi: 10.1038/nature03132; pmid: 15592414
93. D. Contreras, A. Destexhe, T. J. Sejnowski, M. Steriade, Control of spatiotemporal coherence of a thalamic oscillation by corticothalamic feedback. *Science* **274**, 771–774 (1996). doi: 10.1126/science.274.5288.771; pmid: 8864114
94. R. W. Guillery, S. L. Feig, D. A. Lozsádi, Paying attention to the thalamic reticular nucleus. *Trends Neurosci.* **21**, 28–32 (1998). doi: 10.1016/S0166-2236(97)01157-0; pmid: 9464683
95. D. A. McCormick, T. Bal, Sleep and arousal: Thalamocortical mechanisms. *Annu. Rev. Neurosci.* **20**, 185–215 (1997). doi: 10.1146/annurev.neuro.20.1.185; pmid: 9056712
96. S. Palva, J. M. Palva, New vistas for α-frequency band oscillations. *Trends Neurosci.* **30**, 150–158 (2007). doi: 10.1016/j.tins.2007.02.001; pmid: 17307258
97. M. Steriade, D. A. McCormick, T. J. Sejnowski, Thalamocortical oscillations in the sleeping and aroused brain. *Science* **262**, 679–685 (1993). doi: 10.1126/science.8235588; pmid: 8235588
98. Y. Li *et al.*, Distinct subnetworks of the thalamic reticular nucleus. *Nature* **583**, 819–824 (2020). doi: 10.1038/s41586-020-2504-5; pmid: 32699411
99. L. D. Lewis *et al.*, Thalamic reticular nucleus induces fast and local modulation of arousal state. *eLife* **4**, e08760 (2015). doi: 10.7554/eLife.08760; pmid: 26460547
100. Y.-W. Lam, S. M. Sherman, Functional organization of the thalamic input to the thalamic reticular nucleus. *J. Neurosci.* **31**, 6791–6799 (2011). doi: 10.1523/JNEUROSCI.3073-10.2011; pmid: 21543609
101. N. Hádinger *et al.*, Region-selective control of the thalamic reticular nucleus via cortical layer 5 pyramidal cells. *Nat. Neurosci.* **26**, 116–130 (2023). doi: 10.1038/s41593-022-01217-z; pmid: 36550291
102. D. Pinault, The thalamic reticular nucleus: Structure, function and concept. *Brain Res. Brain Res. Rev.* **46**, 1–31 (2004). doi: 10.1016/j.brainresrev.2004.04.008; pmid: 15297152
103. S. N. Baker, Oscillatory interactions between sensorimotor cortex and the periphery. *Curr. Opin. Neurobiol.* **17**, 649–655 (2007). doi: 10.1016/j.conb.2008.01.007; pmid: 18339546
104. R. De Filippo, D. Schmitz, Differential ripple propagation along the hippocampal longitudinal axis. *eLife* **12**, e85488 (2023). doi: 10.7554/eLife.85488; pmid: 37052307
105. M. Okun, N. A. Steinmetz, A. Lak, M. Dervinis, K. D. Harris, Distinct structure of cortical population activity on fast and infraslow timescales. *Cereb. Cortex* **29**, 2196–2210 (2019). doi: 10.1093/cercor/bhz023; pmid: 30796825
106. S. Haziza *et al.*, Imaging high-frequency voltage dynamics in multiple neuron classes of behaving mammals. *Cell* **188**, 4401–4423.e31 (2025). doi: 10.1016/j.cell.2025.06.028; pmid: 40675148
107. J. Reimer *et al.*, Pupil fluctuations track fast switching of cortical states during quiet wakefulness. *Neuron* **84**, 355–362 (2014). doi: 10.1016/j.neuron.2014.09.033; pmid: 25374359
108. K. Takahashi, M. Saleh, R. D. Penn, N. G. Hatsopoulos, Propagating waves in human motor cortex. *Front. Hum. Neurosci.* **5**, 40 (2011). doi: 10.3389/fnhum.2011.00040; pmid: 21629859
109. C. Stringer *et al.*, Spontaneous behaviors drive multidimensional, brainwide activity. *Science* **364**, 255 (2019). doi: 10.1126/science.aav7893; pmid: 31000656
110. S. Musall, M. T. Kaufman, A. L. Juavinett, S. Gluf, A. K. Churchland, Single-trial neural dynamics are dominated by richly varied movements. *Nat. Neurosci.* **22**, 1677–1686 (2019). doi: 10.1038/s41593-019-0502-4; pmid: 31551604
111. B. C. Talluri *et al.*, Activity in primate visual cortex is minimally driven by spontaneous movements. *Nat. Neurosci.* **26**, 1953–1959 (2023). doi: 10.1038/s41593-023-01459-5; pmid: 37828227
112. J. P. Liska *et al.*, Running modulates primate and rodent visual cortex differently. *eLife* **12**, RP87736 (2024). doi: 10.7554/eLife.87736.3; pmid: 39560660
113. G. Buzsáki, *The Brain from Inside Out* (Oxford Univ. Press, 2019). .doi: 10.1093/oso/9780190905385.001.0001
114. M. S. A. Graziano, Ethological action maps: A paradigm shift for the motor cortex. *Trends Cogn. Sci.* **20**, 121–132 (2016). doi: 10.1016/j.tics.2015.10.008; pmid: 26628112
115. M. Okun *et al.*, Diverse coupling of neurons to populations in sensory cortex. *Nature* **521**, 511–515 (2015). doi: 10.1038/nature14273; pmid: 25849776
116. L. Muller, P. S. Churchland, T. J. Sejnowski, Transformers and cortical waves: Encoders for pulling in context across time. *Trends Neurosci.* **47**, 788–802 (2024). doi: 10.1016/j.tins.2024.08.006; pmid: 39341729
117. T. A. Keller, L. Muller, T. Sejnowski, M. Welling, Traveling waves encode the recent past and enhance sequence learning. arXiv:2309.08045 [Preprint] (2024).
118. R. VanRullen, Perceptual Cycles. *Trends Cogn. Sci.* **20**, 723–735 (2016). doi: 10.1016/j.tics.2016.07.006; pmid: 27567317
119. P. Zatka-Haas, N. A. Steinmetz, M. Carandini, K. D. Harris, Sensory coding and the causal impact of mouse cortex in a visual decision. *eLife* **10**, e63163 (2021). doi: 10.7554/eLife.63163; pmid: 34328419
120. N. A. Steinmetz *et al.*, Aberrant cortical activity in multiple GCaMP6-expressing transgenic mouse lines. *eNeuro* **4**, ENEURO.0207-17.2017 (2017). doi: 10.1523/ENEURO.0207-17.2017; pmid: 28932809
121. N. A. Steinmetz *et al.*, Neuropixels 2.0: A miniaturized high-density probe for stable, long-term brain recordings. *Science* **372**, eabf4588 (2021). doi: 10.1126/science.abf4588; pmid: 33859006

122. D. Birman, K. J. Yang, S. J. West, B. Karsh, Y. Browning, J. H. Siegle, N. A. Steinmetz; International Brain Laboratory, Pinpoint: Trajectory planning for multi-probe electrophysiology and injections in an interactive web-based 3D environment. bioRxiv 548952 [Preprint] (2023); https://doi.org/10.1101/2023.07.14.548952.
123. N. Renier *et al.*, iDISCO: A simple, rapid method to immunolabel large tissue samples for volume imaging. *Cell* **159**, 896–910 (2014). doi: 10.1016/j.cell.2014.10.010; pmid: 25417164
124. H. Bokil, P. Andrews, J. E. Kulkarni, S. Mehta, P. P. Mitra, Chronux: A platform for analyzing neural signals. *J. Neurosci. Methods* **192**, 146–151 (2010). doi: 10.1016/j.jneumeth.2010.06.020; pmid: 20637804
125. A. Mathis *et al.*, DeepLabCut: Markerless pose estimation of user-defined body parts with deep learning. *Nat. Neurosci.* **21**, 1281–1289 (2018). doi: 10.1038/s41593-018-0209-y; pmid: 30127430
126. B. K. P. Horn, B. G. Schunck, Determining optical flow. *Artif. Intell.* **17**, 185–203 (1981). doi: 10.1016/0004-3702(81)90024-2
127. W. Gilpin, M. S. Bull, M. Prakash, The multiscale physics of cilia and flagella. *Nat. Rev. Phys.* **2**, 74–88 (2020). doi: 10.1038/s42254-019-0129-0
128. J. D. Semedo, E. Gokcen, C. K. Machens, A. Kohn, B. M. Yu, Statistical methods for dissecting interactions between brain areas. *Curr. Opin. Neurobiol.* **65**, 59–69 (2020). doi: 10.1016/j.conb.2020.09.009; pmid: 33142111
129. Z. Ye, zhiwen10/YE-et-al-2023-spirals: Brain-wide topographic coordination of rotating waves, Zenodo (2026); .doi: 10.5281/zenodo.18781043

ACKNOWLEDGMENTS

We thank S. Grødem, K. Lensjø, and M. Fyhn for the jGCaMP8 viruses; S. Golden for lightsheet imaging support; and B. Brunton, K. Harris, R. Raut, H. Gurnani, and members of the Steinmetz lab for discussions about this work. **Funding:** This work was supported by the National Science Foundation (CAREER award 2142911 to N.A.S.), the Pew Biomedical Scholars Program (N.A.S.), a Klingenstein-Simons Fellowship in Neuroscience (N.A.S.), the National Institutes of Health (NIH BRAIN Initiative grant U19MH114830 to H.Z.), the Washington Research Foundation (a postdoctoral fellowship to D.B.), and the National Eye Institute of the NIH (postdoctoral support grant NEI T32 EY07031 to D.B.). **Author contributions:** Animal husbandry: L.K.; Ai195 and Ai210 transgenic mouse lines: T.L.D. and B.T.; Computational modeling: Z.Y., A.E.L., N.M., M.S.B., N.A.S; Conceptualization: Z.Y. and N.A.S.; Data analysis: Z.Y.; Data collection: Z.Y.; Funding: primary funding acquisition, N.A.S., and funding acquisition for creating transgenic mouse lines, H.Z.; Imaging protocols: Z.Y., A.J.L., D.B.; Supervision: Z.Y., N.A.S; Writing – original draft: Z.Y., N.A.S.; Writing – review & editing: Z.Y., A.E.L., N.M., M.S.B., D.B., N.A.S.; **Competing interests:** H.Z. is on the scientific advisory board of MapLight Therapeutics, Inc. The remaining authors declare no competing interests. **Data, code, and materials availability:** All data are available from: https://doi.org/10.6084/m9.figshare.27850707. A detailed data description and companion code are at: https://github.com/zhiwen10/YE-et-al-2023-spirals, which have been permanently archived in Zenodo (*129*). Ai195 and Ai210 mouse lines are available from The Jackson Laboratory (#034112 and #037378), subject to their "general terms and conditions."

SUPPLEMENTARY MATERIALS

science.org/doi/10.1126/science.adx1369
Figs. S1 to S15; Tables S1 and S2; Movie S1; MDAR Reproducibility Checklist
Submitted 3 March 2025; resubmitted 13 November 2025; accepted 8 April 2026
10.1126/science.adx1369

Brain-wide topographic coordination of rotating waves

Zhiwen Ye, Alexander E. Ladd, Nancy MacKenzie, Ljuvica Kolich, Anna J. Li, Daniel Birman, Matthew S. Bull, Tanya L. Daigle, Bosiljka Tasic, Hongkui Zeng, and Nicholas A. Steinmetz

Science **392** (6804), eadx1369. DOI: 10.1126/science.adx1369

Editor's summary

Waves of brain activity (traveling waves) have been observed in many species. Given their prevalence and magnitude, it has been hypothesized that these waves likely play an important role in the brain. However, their functions remain to be elucidated. Ye *et al*. used wide-field calcium imaging to study traveling waves in the mouse neocortex. Traveling waves coincided with the recruitment of spiking activity in connected subcortical structures and were well coordinated between the two hemispheres. The arrangement of local axons in the sensory cortex followed the shape of the traveling waves. These results open new avenues of inquiry into the mechanisms underlying traveling waves and their function. —Mattia Maroso

Science (ISSN 1095-9203) is published by the American Association for the Advancement of Science. 1200 New York Avenue NW, Washington, DC 20005. The title *Science* is a registered trademark of AAAS.